Bond behavior of near-surface mounted CFRP laminate strips under monotonic and cyclic loading

José Sena Cruz, Joaquim Barros and Ravindra Gettu

Report 04-DEC/E-04

Technical report developed as part of the doctoral degree requirements of José Manuel de Sena Cruz

Date: January 2004
N. of pages: 55
Keywords: Bond, slip, bond stress, CFRP laminate strip, pullout bending test

Escola de Engenharia | Departamento de Engenharia Civil | Universidade do Minho | Structural Technology Laboratory | Universitat Politecnica de Catalunya

INDEX

1 INTRODUCTION 3

2 EXPERIMENTAL PROGRAM 4
2.1 Specimen configuration 4
2.2 Measuring devices 5
2.3 Test program 5

3 MATERIAL PROPERTIES 7
3.1 Concrete 7
3.2 CFRP laminate 10
3.2.1 Geometrical properties 11
3.2.2 Mechanical properties 12
3.3 Epoxy-adhesive 14
3.3.1 Mechanical properties 14

4 PULLOUT-BENDING TESTS 17
4.1 Specimen preparation 17
4.2 Monotonic loading results 19
4.2.1 Visual observations and failure mode 19
4.2.2 Pullout load 19
4.2.3 Slip at free and loaded ends 26
4.2.4 Pullout force vs. slip 27
4.2.5 Bond stress vs. slip 29
4.2.6 Discussion of results 29
4.3 Cyclic loading results 32
4.3.1 Free end slip, loaded end slip and pullout force 32
4.3.2 Pullout force vs. slip 33
4.3.3 Bond stress vs. slip 34
4.3.4 Discussion of results 36

5 CONCLUSIONS 39

6 ACKNOWLEDGEMENTS 40

7 REFERENCES 40

APPENDIX I 42

APPENDIX II 43

1 INTRODUCTION

In recent years, the Near-Surface Mounted (NSM) strengthening technique has been used to increase the load carrying capacity of concrete and masonry structures. This technique consists of bonding Carbon Fiber Reinforced Polymer (CFRP) laminate strips within pre-cut grooves on the concrete cover of the elements to be strengthened. From the results of previous experimental programs (Ferreira 2000, Barros and Fortes 2002, Barros and Dias 2003), high levels of strengthening efficacy with concrete columns, beams and masonry panels can be achieved. This technique does not require surface preparation and, after cutting the groove, requires minimal installation time compared to the Externally Bonded Reinforcing (EBR) technique. A further advantage associated with NSM with CFRP is its ability to significantly reduce the probability of harm resulting from fire, acts of vandalism, mechanical damages and aging effects.

To characterize the bond behavior of the laminate to concrete under monotonic loading, pullout-bending tests were carried out (Sena-Cruz and Barros 2002a, b). The pullout force at the laminate, and the slip at the free and loaded ends were measured. The influences of the concrete strength and bond length on the bonding behavior between these two materials were analyzed. From the obtained results, the following remarks can be made:

- The failure always occurred by pullout of the laminate;
- The bond strength attained values significantly higher than the ones obtained when using EBR strengthening technique;
- The peak pullout force and the corresponding slip increased with the bond length;
- The bond strength revealed a tendency to decrease with the increase of the bond length;
- The influence of the concrete strength on the main parameters analyzed (pullout force, bond strength, ratio between the maximum stress and the tensile strength of the CFRP, and the loaded end slip at peak pullout load) was negligible;
- The evolution of the bond stress and the slip along the bond length is essentially nonlinear.

To assess the bond behavior between concrete and laminate under monotonic and cyclic loadings another research program was carried out, using a pullout-bending test setup similar to the one used to characterize the bond behavior of the laminate to concrete

under monotonic loading. Maintaining the same groove size, the epoxy adhesive and the concrete strength in the experimental program, the influences of both the bond length and the loading history on the bond behavior were analyzed.

The experimental work was developed in the Structural Technology Laboratory of the *Universitat Politecnica de Catalunya*, Barcelona, Spain. The present report describes the tests carried out, and analyses the main results.

2 EXPERIMENTAL PROGRAM

2.1 Specimen configuration

The test layout adopted is similar to the one proposed by RILEM for assessing the bond characteristics of conventional steel rods (RILEM, 1982). The dimensions of the concrete specimen were changed in order to use the available molds.

Figure 1 shows the pullout-bending test adopted in the present work. Blocks A and B are connected through a steel hinge in the top part, and by the CFRP laminate at the bottom.

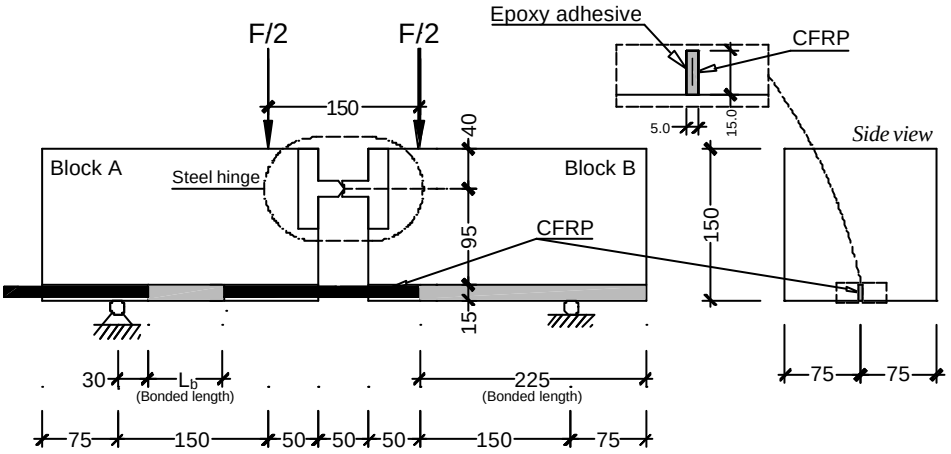

Figure 1 – Specimen geometry and pullout-bending test configuration.

The bond test region was localized in block A, using distinct bond lengths, L_b. To ensure negligible slip of the laminate fixed to block B, a bond length of 225 mm was considered. This also ensures that the bond failure occurs in block A.

2.2 Measuring devices

To measure the slip, two displacement transducers (LVDT1 and LVDT2) of 10 mm nominal stroke were applied (see Figure 2). LVDT2 measured the slip at the loaded end, s_l, while LVDT1 recorded the slip at the free end, s_f. LVDT2 was also used to control the test at 5 μm/s. The applied force, F, was measured using a load cell (±100kN) placed between the specimen top surface and the actuator. One strain gage was glued to the CFRP at the symmetry axis of the specimen was used for the determination of the pullout force on the CFRP at the loaded end. In this program BFLA-5-8 from TML (see http://www.tokyosokki.co.jp/e/index.html, 2003-02-06) and 6/120LY11 from HBM (see http://www.hbm.com, 2003-02-06) strain gages were used.

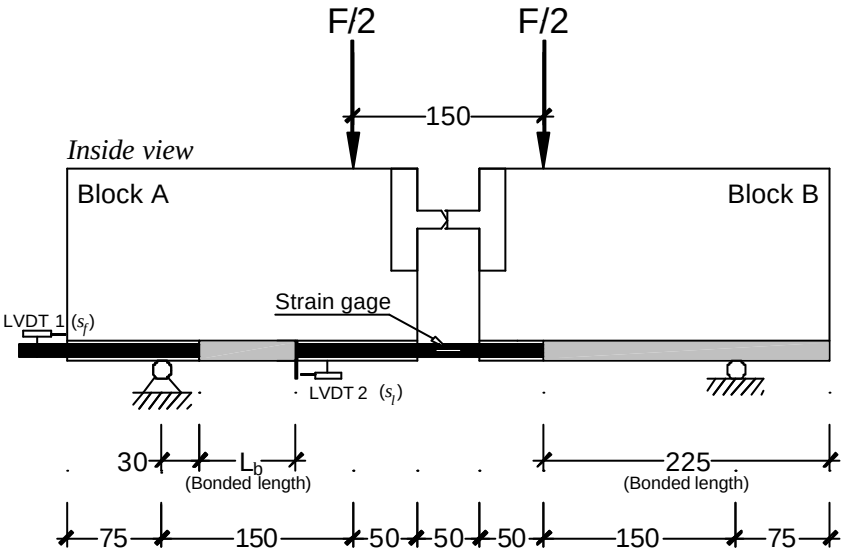

Figure 2 – Measuring devices.

Figure 3 shows the full arrangement of the pullout-bending test. A servo-controlled test machine (Instron, series 8505) was used in the experimental program.

2.3 Test program

In the present experimental program the influence of the bond length and the loading history on the bond behavior was analyzed. Three different bond lengths were used (Lb=60, 90 and 120 mm) and three types of load history were utilized: monotonic loading (denoted as M), 1 cycle of loading/unloading at different deflection levels (denoted as C1)

and 10 cycles of loading/unloading for a fixed load level (denoted as C10). Table 1 includes the denomination of the different series, each one consisting of three specimens.

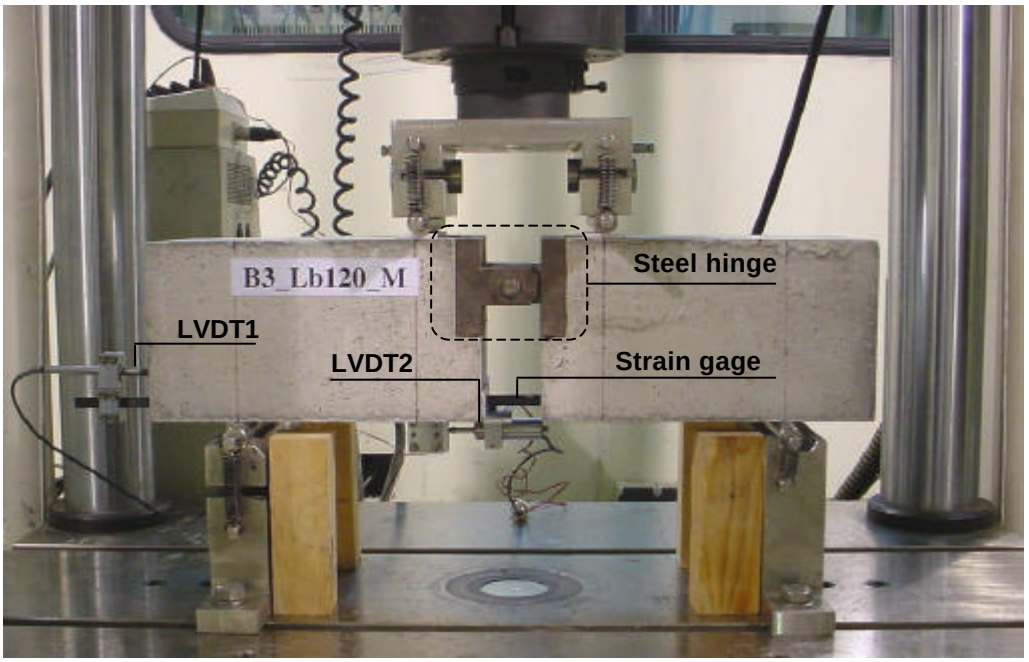

Figure 3 – Layout of the pullout-bending test.

Table 1 – Denomination of the series.

Bond length (mm)	**Load type**	**Denomination**
60	Monotonic (M)	Lb60_M
	Cyclic (C10) [a]	Lb60_C10
90	Monotonic (M)	Lb90_M
	Cyclic (C10) [b]	Lb90_C10
120	Monotonic (M)	Lb120_M
	Cyclic (C10) [c]	Lb120_C10
	Cyclic (C1) [d]	Lb120_C1

[a] 10 cycles at 90% of the bond strength.
[b] 10 cycles at 60% of the bond strength.
[c] 10 cycles at 75% of the bond strength.
[d] 1 cycle at 250μm, 500μm, 750μm, 1000μm, 1500μm, 2000μm, 3000μm, 4000μm

3 MATERIAL PROPERTIES

3.1 Concrete

The granulometric analyses of the sand (0-5 mm) and the gravel (5-12 mm) used in the concrete aggregate skeleton are included in Table 2 and Figure 4. This analysis was carried out according to the recommendations of UNE-EN 933-1. The concrete composition is indicated in Table 3.

To avoid any undesired shear failure of the specimens (Sena-Cruz et al. 2001), 60 kg/m^3 of hooked ends Dramix® RC-80-30 BP steel fibers were added to the concrete.

In the manufacturing of the concrete a 250 liter vertical-axis forced-action mixer was used. The mixing procedures were the following:

- the coarse, fine aggregates and the cement were mixed during 1 minute;
- the water was added and the mix continued during another minute;
- the superplasticizer was incorporated and the mixing continued during another minute;
- the steel fibres were gradually added and the concrete was mixed during another 2 minutes.

The mix had satisfactory homogeneity and no balling of fibers was observed. To evaluate the workability of the fresh concrete, *Slump tests* were carried out, obtaining a slump of 15.0 cm and 16.5 cm in the *C1* and *C2* concrete mixes, respectively.

Table 2 – Results from the granulometric analyses.

Sieve (mm)	Retained material (%)	
	Sand (0-5)	Gravel (5-12)
63	0.0	0.0
31.5	0.0	0.0
16	0.0	0.0
8	0.0	9.0
4	0.5	100.0
2	23.4	100.0
1	53.2	100.0
0.5	75.3	100.0
0.25	95.4	100.0
0.125	99.3	100.0
0.063	99.9	100.0
< 0.063	100	100.0

For each concrete mix, six 150×300 mm cylinders and twenty blocks was cast in two layers each, each compacted on 50Hz-vibrating table during 20 seconds. After filling the molds (see Figure 5 and Figure 6), the top surfaces were finished manually and covered with a plastic sheet. The specimens were taken out of the molds 24 hours after had been cast and were placed in a curing room (at 20±2º C and 98% RH).

Table 3 – Mix composition of the concrete of the series tested.

Cement 52.5 type I (kg)	**Sand (0-5 mm)** (kg)	**Gravel (5-12 mm)** (kg)	**Water** (l)	**Superplasticizer** [a] (% of cement)
350	990	705	203	1.15

[a] Superplasticizer DARACEM® 205 (2001)

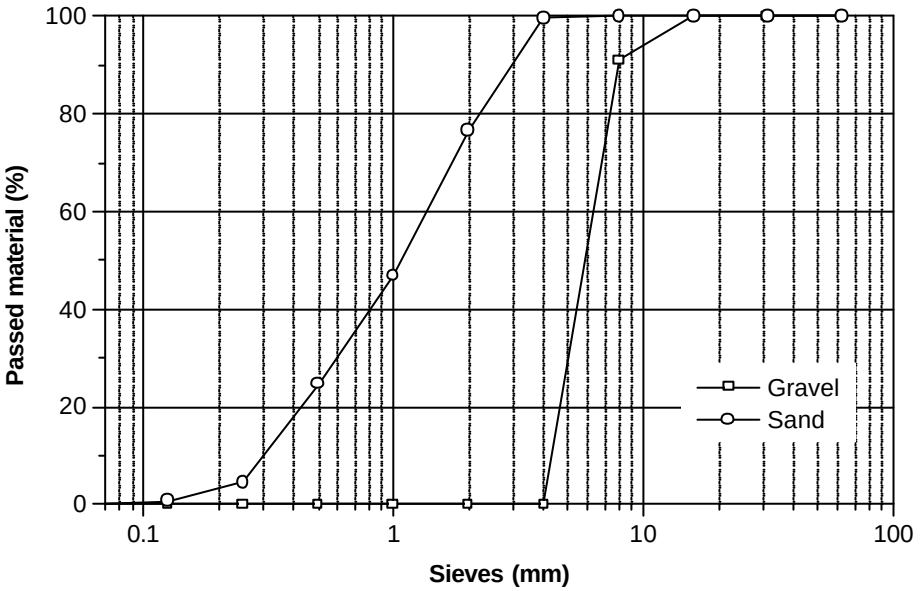

Figure 4 – Granulometric curve.

Figure 5 – Molds used.

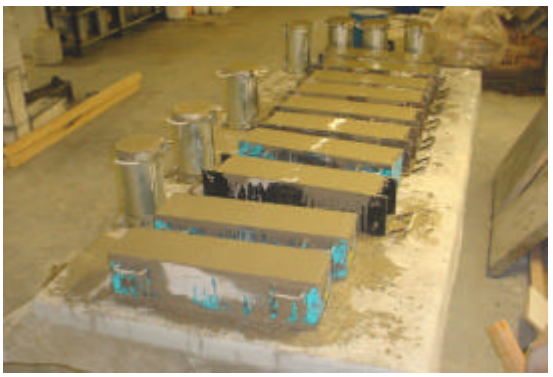

Figure 6 – Specimen's after casting.

To characterize the concrete compression strength, uniaxial compression tests were carried out in a universal testing machine, as shown in Figure 7. Concrete Young's modulus was also obtained (see Figure 8). A stress rate of 0.5 MPa/s was used to control the compression tests. To determine the Young's modulus, E_{ci}, three loading-unloading cycles were executed at stress rate of 0.5 MPa/s. A maximum difference of 0.25% in the E_{ci} values between the second and the third cycles was recorded. The applied stress ranged between 0.5 MPa and 1/3 of the compression strength. The length variation of a central zone of the specimen, with a reference length of 150 mm, was evaluated from three LVDTs placed according to Figure 8 (spaced at 120º between each pair of LVDTs). Figure 9 shows the displacement history registered by the LVDTs in specimen *S4* of the concrete mix *C1*, from which it can be concluded that the equipment used has enough accuracy to evaluate the Young's modulus. The strain was obtained dividing the average value of the displacements measured in the three LVDTs by the reference length. The Young's modulus was determined from linear regression analysis with the largest number of points of the linear-trend-part of the stress-strain curve of the last two loading branches.

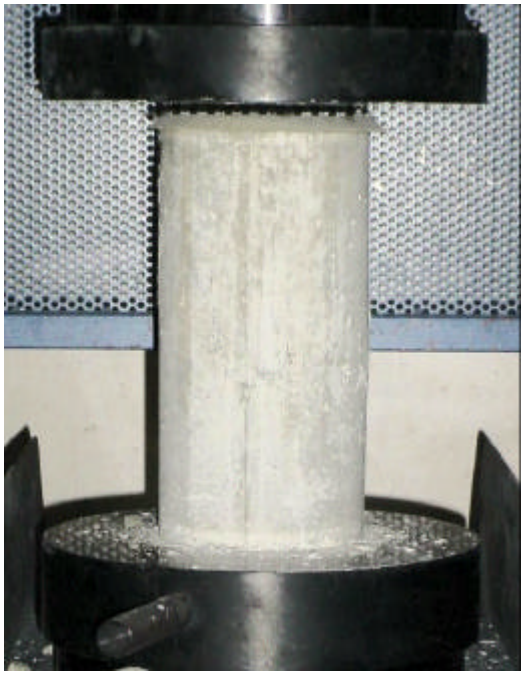

Figure 7 – Compression test.

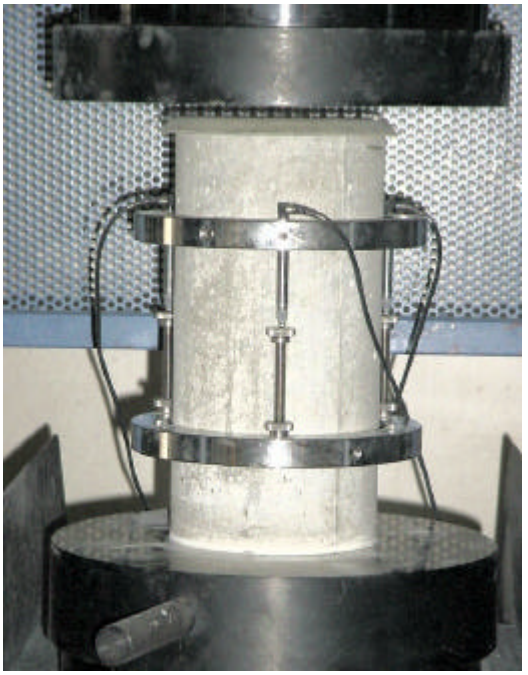

Figure 8 –Young's modulus test.

The compressive strength and the Young's modulus recorded in each specimen of the *C1* and *C2* mixes are included in Table 4. The average values of the strength and

modulus were about 41.0 MPa and 32 GPa, respectively. Low values of the coefficient of variation were registered (represented within parentheses).

Table 4 – Concrete compression strength and Young's modulus results.

Specimen	**Concrete mix** *C1*		**Concrete mix** *C2*	
	f_c (MPa)	E_{ci} (GPa)	f_c (GPa)	E_{ci} (MPa)
S1	40.5	–	41.4	–
S2	40.1	–	39.5	–
S3	40.5	–	40.7	–
S4	41.5	32.0	42.5	32.0
S5	40.5	32.7	40.4	31.1
S6	42.5	32.0	41.5	31.9
Average	40.9 (2.2%)	32.2 (1.2%)	41.0 (2.5%)	31.7 (1.6%)

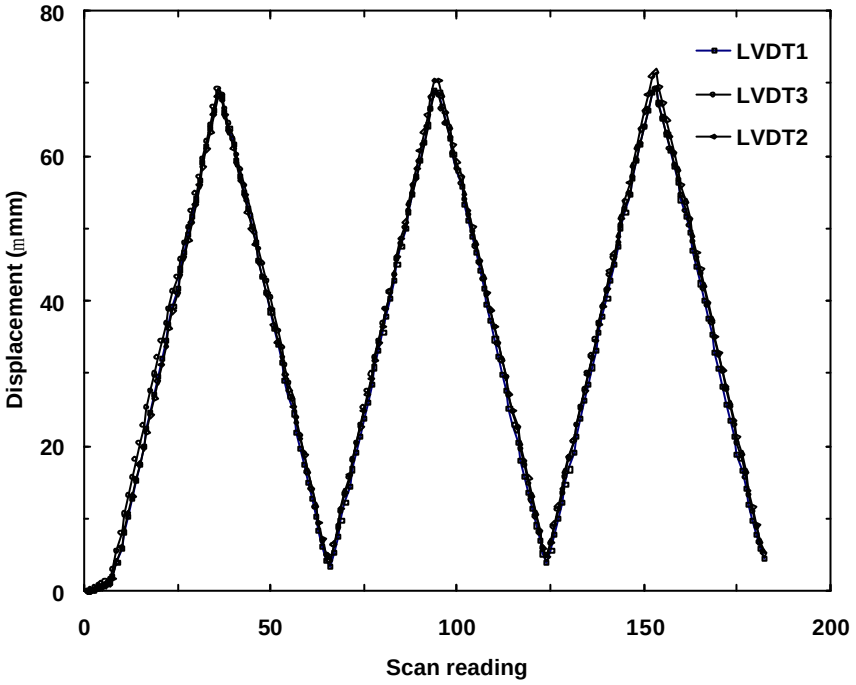

Figure 9 – Typical displacement evolution in the three LVDTs (specimen *S4* of the concrete mix *C1*).

3.2 CFRP laminate

The CFRP laminate was provided in a roll and was produced by S&P® and distributed by Bettor MBT® Spain (see Figure 10). The laminate had the trademark of *MBrace LM* (1999), and was composed by unidirectional carbon fibres, agglutinated by an epoxy adhesive. According to the supplier the *MBrace LM* have the main properties included in

Table 5. The following sections deal with the CFRP geometrical and mechanical properties measured in the laboratory.

Table 5 – Main properties of the *MBrace LM*.

Property	Value
Width (mm)	10.0
Thickness (mm)	1.4
Tensile strength (MPa)	2500
Young's modulus (GPa)	150
Ultimate strain (%)	1.25

Figure 10 – Roll of CFRP laminate.

3.2.1 Geometrical properties

From twenty measurements it was verified that the width and the thickness of the laminate was 10.03±0.014 mm and 1.40±0.007 mm, respectively. In the following sections the values of 10.03 mm and 1.40 mm for the width (w_f) and thickness (t_f) of the laminate, are respectively considered.

3.2.2 Mechanical properties

To evaluate the tensile strength and the Young's modulus of the laminate, uniaxial tensile tests were carried out in a servo-controlled test machine (Instron, series 8505), according to the recommendations of ISO 527-5 (1997).

The specimens had a length of 250 mm and, tabs were glued at the ends to avoid premature failure due to stress concentrations by the machine fixtures (see Figure 11). The end-tabs were made with the same material. The test was controlled at a constant displacement rate of 2 mm/min. Strain gages were used to evaluate the strain of the laminate. The applied force was measured using a load cell of a static load carrying capacity of ±100 kN. Figure 12 shows the test layout.

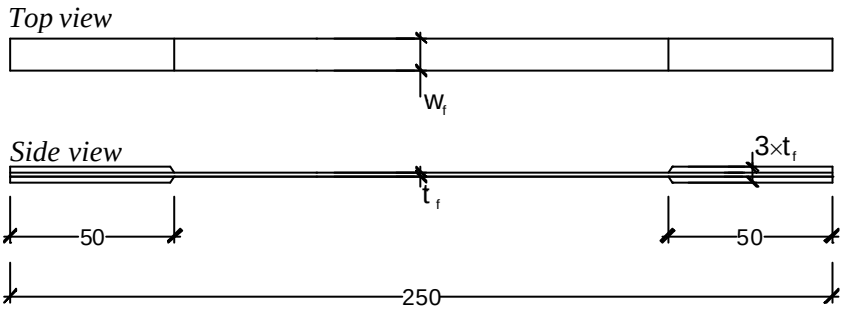

Figure 11 – Geometry of the CFRP specimen.

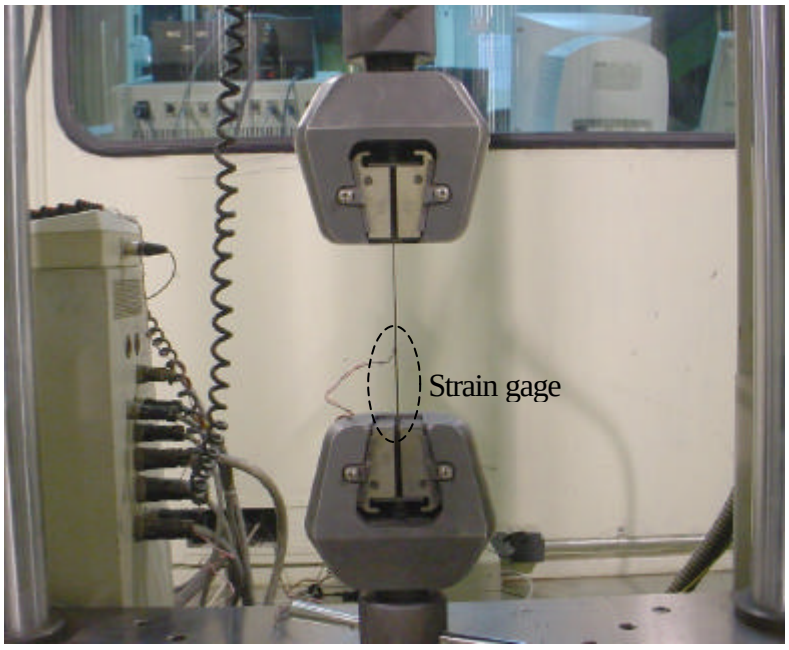

Figure 12 – Layout of the CFRP tensile tests.

At about 75% of the ultimate tensile strength, fibers began rupturing with a strident audible sound. The failure occurred in a very brittle fashion with a loud sound. Figure 13 shows the appearance of the specimens after they had been tested. In some specimens the failure region did not occur at the central part of the specimen. This can be justified by the difficulty on ensuring homogeneity in the fiber distribution, fiber alignment and laminate cross sectional area.

Figure 13 – Failure of the CFRP specimens.

Figure 14 represents the stress-strain relationship obtained in the five tested specimens. A linear strain-stress relationship up to peak load can be observed. Table 6 includes the tensile strength, Young's modulus and ultimate strain (at the peak stress) of each specimen. Low values of coefficient of variation were obtained. In the following sections, the values of 2800 MPa, 171 GPa and 1.55%, will be considered, respectively, for the tensile strength (f_{fu}), Young's modulus (E_f) and ultimate strain ($e_{f\max}$).

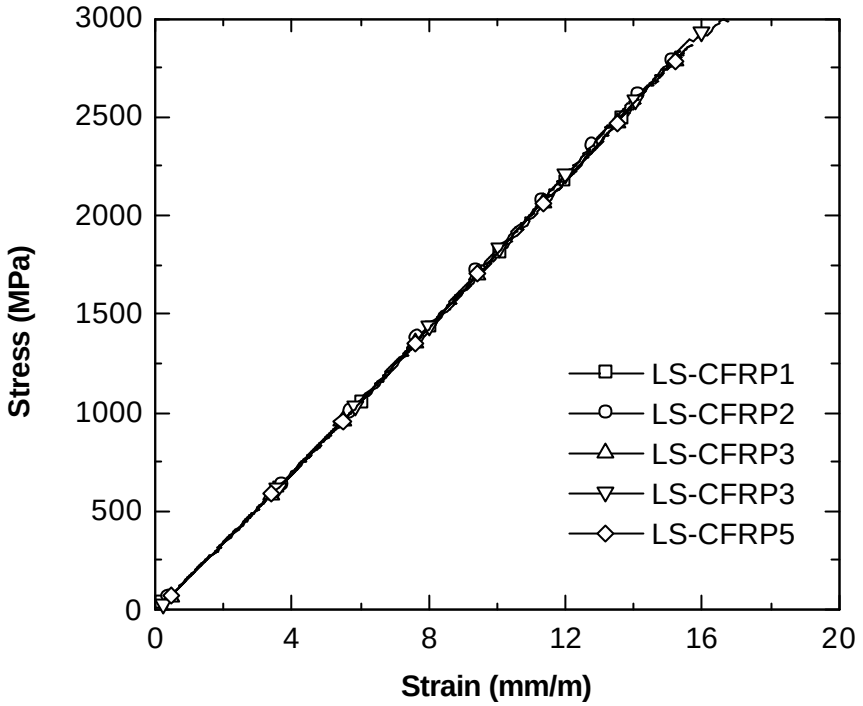

Figure 14 – Stress-strain relationship of the specimens analyzed.

Table 6 – Results from the tensile tests with specimen of the CFRP laminate.

Specimen	**Tensile strength** (MPa)	**Young's modulus** (GPa)	**Ultimate strain** (%)
LS-CFRP1	2570	169.3	1.40
LS-CFRP2	2819	170.0	1.54
LS-CFRP3	2862	171.4	1.57
LS-CFRP4	2993	172.9	1.67
LS-CFRP5	2922	172.0	1.58
Average	2833 (5.7%)	171.1 (0.85%)	1.55 (6.2%)

3.3 Epoxy-adhesive

The low viscosity epoxy adhesive used to bond the CFRP laminate to concrete had the trademark *Mbrace Epoxikleber 220*. This adhesive was composed of two parts (A and B) and was available in packs of 12 kg (9 kg + 3 kg) (see Figure 15). According to the supplier the epoxy adhesive have the properties indicated in Table 7.

3.3.1 Mechanical properties

To characterize the epoxy adhesive, three point bending tests and compression tests were carried out according to the recommendations of NP196-1 (1990).

Figure 15 – *Mbrace Epoxikleber 220*: part A and part B.

Table 7 – Main properties of *Mbrace Epoxikleber 220*.

Property	Value
Density (g/cm^3)	1.7
Compressive strength (MPa)	40.0
Tensile strength (MPa)	7.0
Young's modulus (GPa)	7.0
Bond strength to concrete (MPa)	3.0
Bond strength to CFRP laminate (MPa)	3.0
Pot life at 20ºC (min)	60
Time of cure (days)	3
Mixing ratio (Part A to Part B)	3 to 1 by weight

To manufacture epoxy specimens of 160×40×40 mm^3 the following steps were taken: the two components were homogenized individually; component B was added to the component A and during 2 minutes they were mixed together in a mixer machine of 1800 rpm; the procedure was interrupted in order to homogenize the mix, using a spoon; the mixing procedure continued during more two minutes. This procedure ensured mixtures with the desired quality. The molds were cast in two layers, each compacted by 120 jolts. The specimens were removed from the moulds 24 hours after have been cast and were placed into an environmental chamber (at 20º C and 50% RH).

The bending tests were conducted in a universal test machine under load control at a rate of 50 N/s (see Figure 16). The appearance of the specimen after it had been tested is

shown in Figure 17. Several voids were observed in the fracture surface of the specimens, which can be responsible for the large coefficient of variation obtained (value in parentheses) and reported in Table 8.

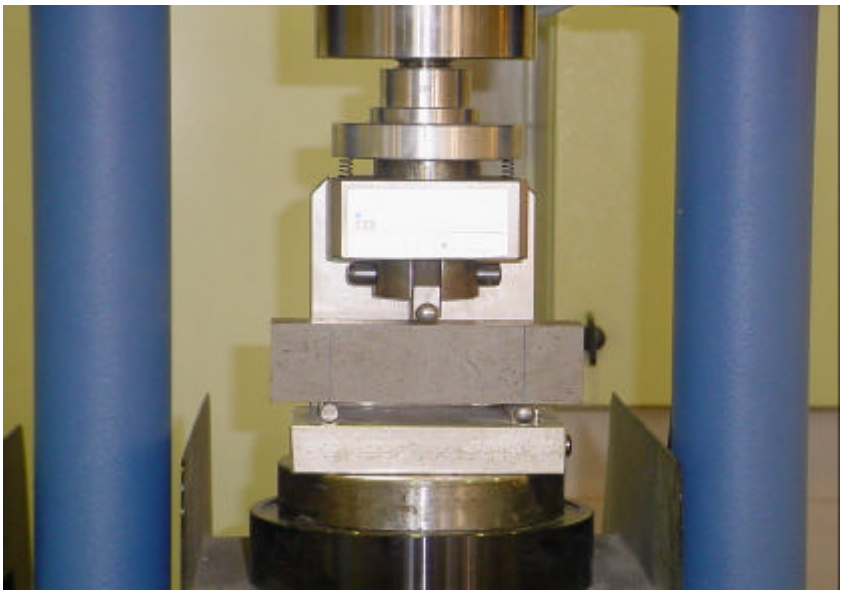

Figure 16 – Layout of three point bending tests with epoxy adhesive specimens.

Compression tests were carried out with the two parts resulting from the prismatic specimens after they had been tested in bending. The compression tests were conducted in a universal testing machine under load control at a rate of 2.4 kN/s (see Figure 18). From six tests, an average compressive strength of 67.5 MPa was obtained with a coefficient of variation of 5.3%.

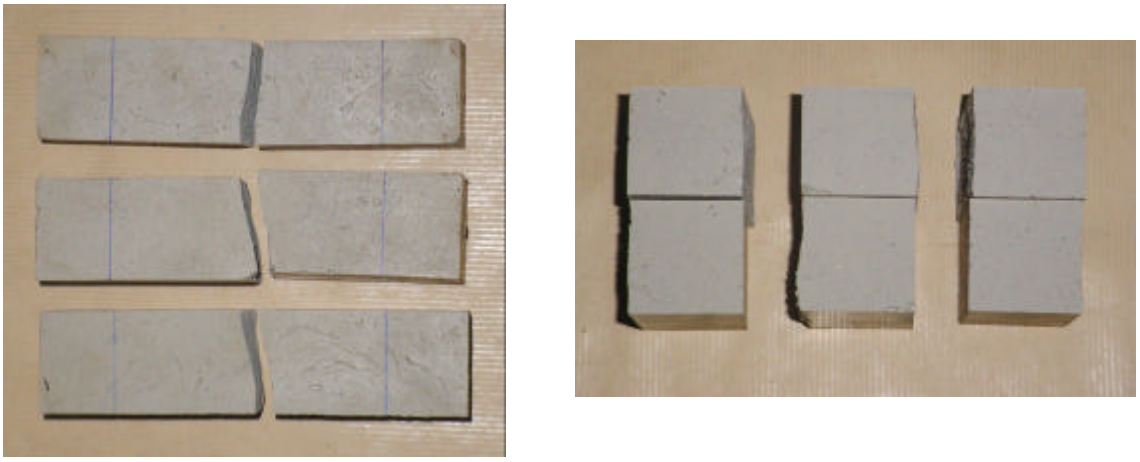

(a) (b)

Figure 17 – Failure of the tested specimens: (a) lateral view; (b) top view.

Table 8 – Results from the three point bending tests of epoxy adhesive specimens.

Specimen	**Flexural tensile strength** (MPa)
B1	28.0
B2	19.3
B3	17.9
Average	21.8 (25.2%)

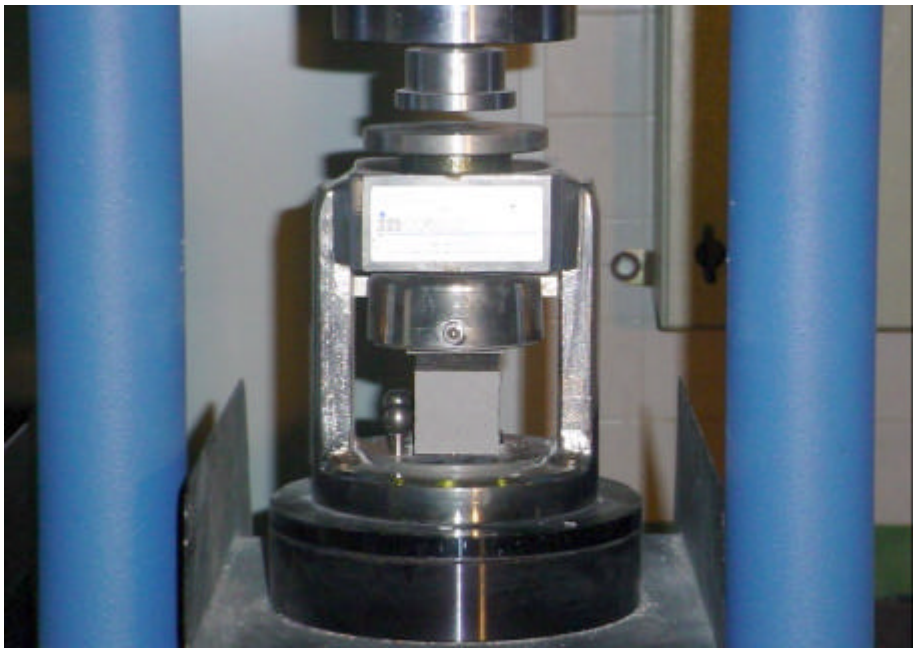

Figure 18 – Layout of compression tests with epoxy adhesive specimens.

Table 9 – Results from the compression tests on the epoxy adhesive specimens.

Specimen	**Compressive strength** (MPa)
B1-A	66.0
B1-B	64.5
B2-A	64.8
B2-B	72.4
B3-A	65.5
B3-B	71.8
Average	67.5 (5.3%)

4 PULLOUT-BENDING TESTS

4.1 Specimen preparation

Figure 19 includes the main steps used in the preparation of a pullout-bending specimen. In the following paragraphs these steps are described in detail.

At the age of 28 days the two blocks composing each specimen (see Figure 1) were removed from the curing room to make the grooves using a table-mounted saw (Figure 20 (a)). In order to eliminate the dust from the sawing process, the grooves were cleaned with water under pressure (Figure 20 (b)). To ensure a dry surface before bonding the laminate to the concrete, the specimens were air-dried in the laboratory environment during two weeks.

Prior to CFRP installation, the width and the depth of the groove size, in the test region, were measured. The values are included in Table I.1 (see Appendix I). The depth and the width were, 14.72±0.28 mm and 4.79±0.12 mm, respectively.

Before bonding the CFRP, the grooves were again cleaned by compressed air (see Figure 20 (c)). To avoid epoxy adhesive in undesirable zones, a masking procedure was adopted, as shown in the Figure 20 (d). In the preparation of CFRP, the following were the steps involved:

- a small tab, made with the same CFRP material, was fixed at the loaded end to measure the loaded end slip (see Figure 20 (e));
- small plastics pieces were fixed at the free and loaded ends of the bonded zone in order to ensure the desired length of the test region (see Figure 20 (e));
- the CFRP was cleaned using acetone;
- a strain gage was glued on the CFRP at the mid span of the specimen (see Figure 20 (f));
- finally, in the bonded zones, the CFRP was again cleaned using acetone.

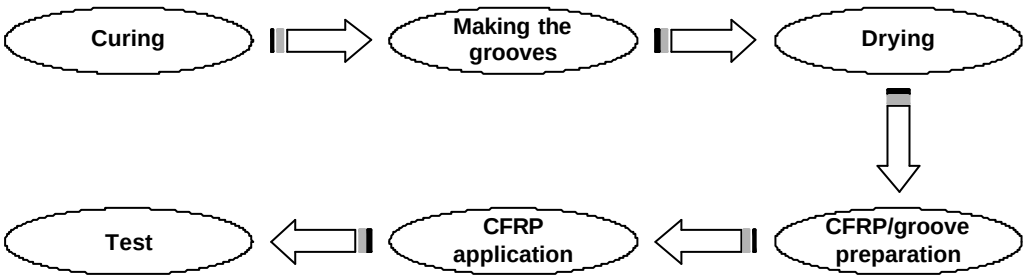

Figure 19 – Main steps used in the preparation of the specimen.

The laminate was fixed to concrete using the epoxy-adhesive described in the Section 3.3.1. In the regions where the CFRP was bonded to concrete, the groove was filled with the epoxy adhesive and the lateral faces of the CFRP were covered by a thin layer of the epoxy adhesive (see Figure 20(g) and (h)). Then, the CFRP was inserted into the groove and was slightly pressed to force the epoxy adhesive to flow between the CFRP and the groove sides. Finally, excess epoxy was removed and the surface was leveled. Figure 21 shows the final condition of the specimens. The specimens remained in the laboratory environment for two months before being tested.

4.2 Monotonic loading results

4.2.1 Visual observations and failure mode

To detect the occurrence of eventual cracks on the concrete, the bonded zone was painted white (see Figure 21). Cracks on the concrete surface, however, were never observed. The failure always occurred in the laminate-adhesive-concrete bonding zone. More details of the failure pattern is described elsewhere (Sena-Cruz and Barros 2002a).

4.2.2 Pullout force

To evaluate the pullout load on the CFRP (at the loaded end of the bond length), F_l, two different approaches were adopted. The first one uses the loads measured with the load cell (F) and takes into account the internal lever arm ($b = 102.5$ mm), i.e., the distance between the longitudinal axis of the CFRP and the center of the steel hinge (see Figure 1), resulting in

$$F_l = \frac{150\, F/2}{b} = F_{leq} \qquad \text{(Eq. 1)}$$

The second approach uses the strain values recorded by the strain gage glued on the CFRP laminate (e_f) and the values of $E_f = 171$GPa and $A_f = 14.04$ mm^2 for the Young's modulus and the cross sectional area of the CFRP, respectively, resulting in

$$F_l = E_f e_f A_f = F_{lsg} \quad \text{(Eq. 2)}$$

(a)

(b)

(c)

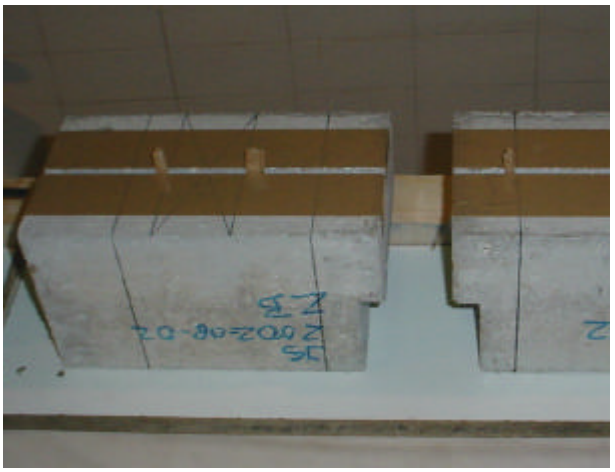

(d)

(e)

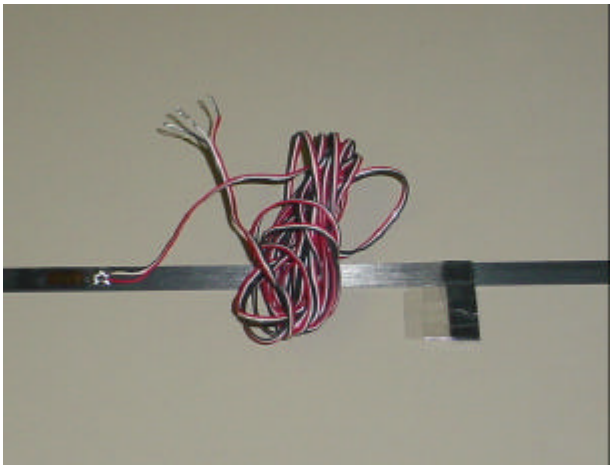

(f)

Figure 20 – Specimen preparation: (a) making the grooves; (b) cleaning the grooves with water under pressure; (c) cleaning the grooves using compressed air; (d) specimen final state before the reinforcement; (e) final state of the laminate bond zone; (f) final state of the CFRP laminate.

(g)

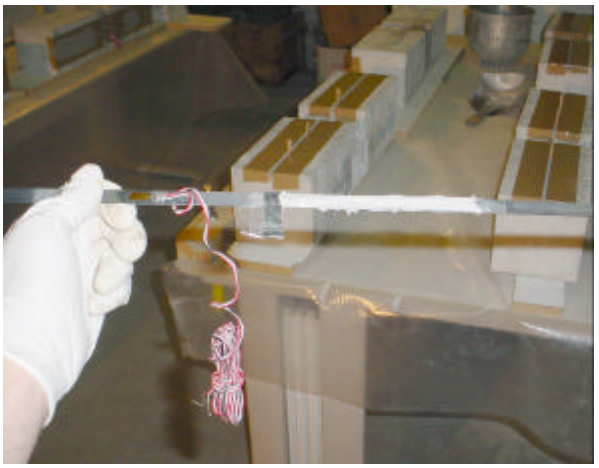

(h)

Figure 20 (Cont.) – Specimen preparation: (g) groove filled with the epoxy; (h) epoxy on the CFRP surface at the bond zone.

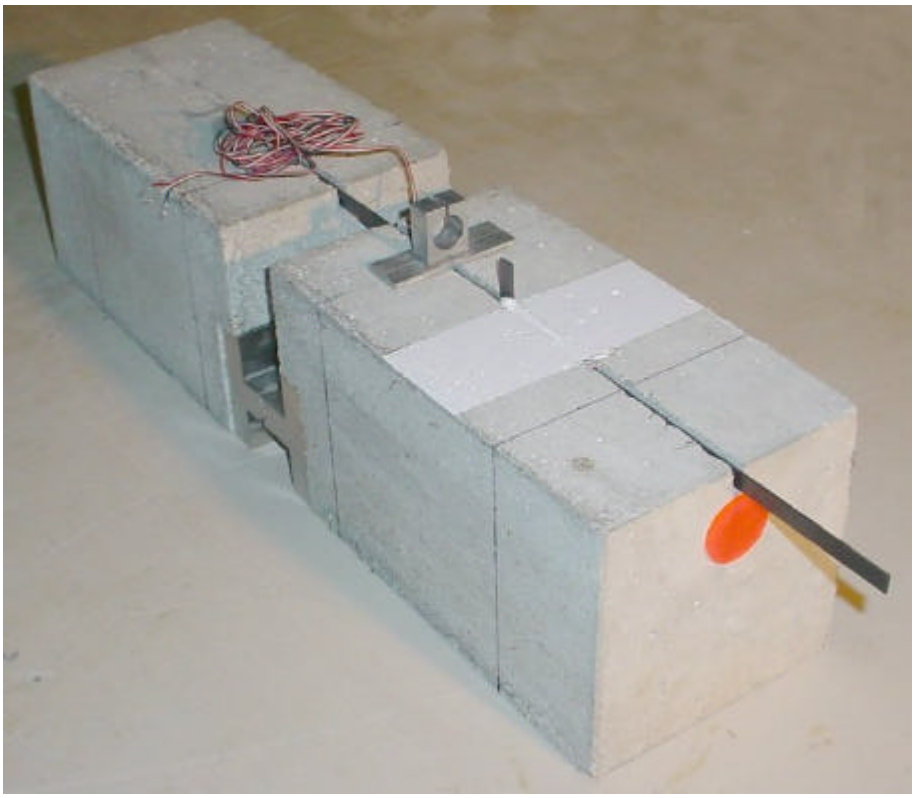

Figure 21 – Final state of the reinforced specimen.

Figure 22 (a) shows a typical time evolution of the pullout force of the specimen *B3_Lb120_M*, calculated using the first and the second approaches, $F_{l\acute{e}q}$, and $F_{l\acute{s}g}$, respectively. Appendix II includes these relationships for all tested specimens. Figure 22(b) reports the time evolution of the $F_{l\acute{s}g}/F_{l\acute{e}q}$ ratio, from which it can be shown that, up

to the peak load, the difference in the forces derived from the two approaches increases, and remains within between 10% to 20% in the stabilized softening phase.

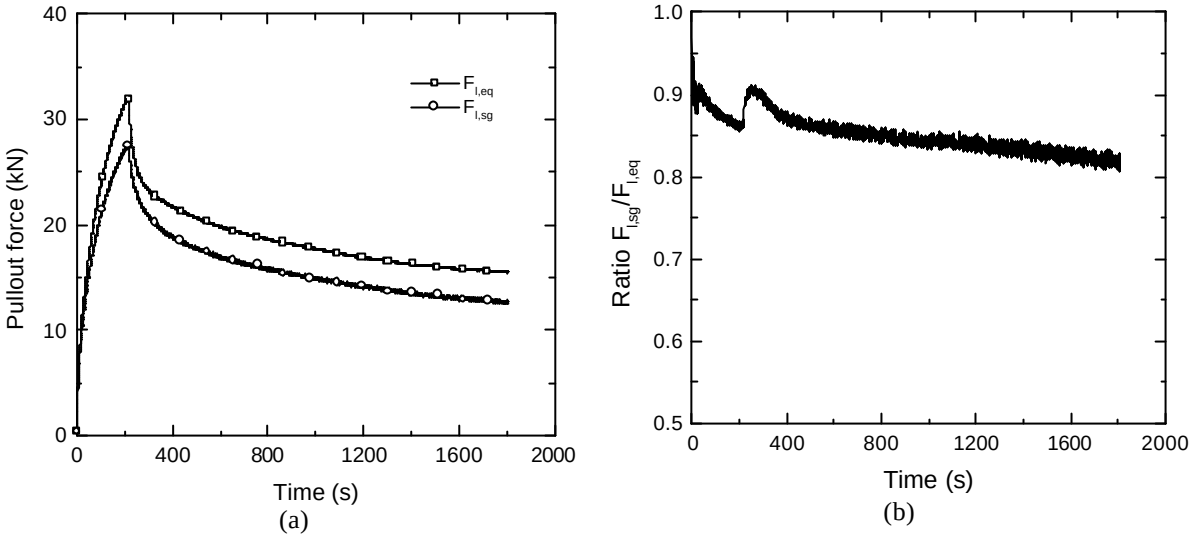

Figure 22 – Time evolution of the pullout force (a) and ratio between F_{leq}/F_{lsg} (b) of the specimen *B3_Lb120_M*.

To assess the reasons than can justify the differences in the force values obtained by these two approaches, the calibration of the load cell and the system used to evaluate the strain were checked, the influence of the variation of the internal arm and the influence of the friction between the specimen and the applying load system were analyzed.

Load cell

The load cell of a static load carrying capacity of ±100 kN used for the experiments is periodically calibrated by Instron technical staff. To certify the calibration, a dynamometric ring (DR) was used, and no significant differences were registered between the values given by the DR and the Instron load cell.

Strain gage

To ascertain if the strain gages were measuring reliable values a clip gage was also used to evaluate the strain (see Figure 23). Similar results were recorded by the strain gage and clip gage (see Figure 24).

Influence of the length variation of the internal lever arm

The variation of the pullout force, ΔF_l, when the internal lever arm (b) of the specimen, i.e., the distance between the CFRP laminate and the steel hinge, has a variation of Δb ($\Delta b > 0$ when the internal arm increases), can be given by:

$$\Delta F_l = -\frac{\Delta b}{b + \Delta b} F_l \qquad \text{(Eq. 3)}$$

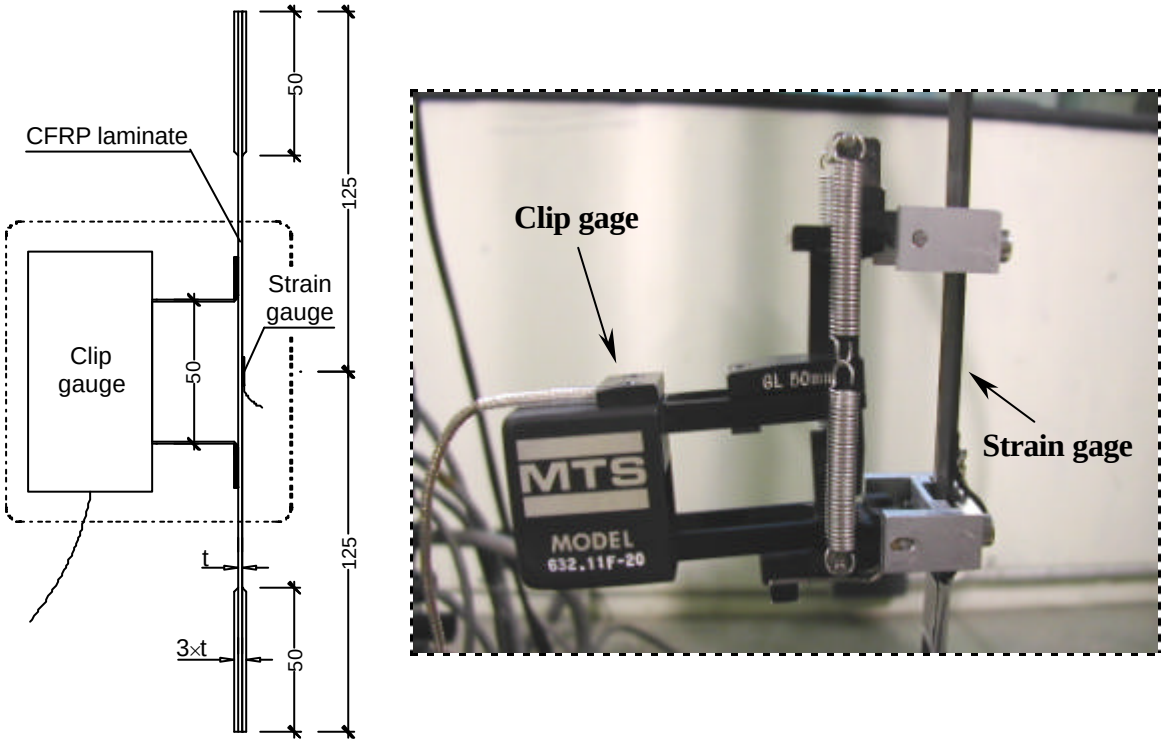

Figure 23 – Geometry and test layout of the CFRP laminate (a); detail of the zone where the displacement/deformation measuring instruments were applied (b).

Figure 25(a) shows the relationship between $\Delta F_l / F_l$ and Δb, for Δb up to 10 mm. During the pullout bending test, the internal lever arm, b, does not remain constant. Figure 26 represents a deformed configuration of the specimen, where it was assumed that the specimen moves like a rigid body and the CFRP laminate remains in its initial position. A variation of 7.4 mm in the internal lever arm was obtained when the point load has deflected 5.0 mm in the vertical direction. For this variation of the internal lever arm, Figure 25(a) shows that a variation of -6.7% of the assumed pullout force is obtained.

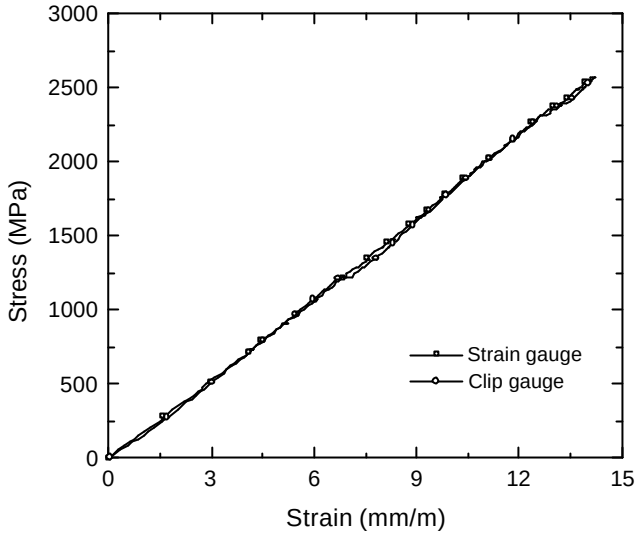

Figure 24 – Stress-strain relationships, where the strain was evaluated using a strain gage and clip gage.

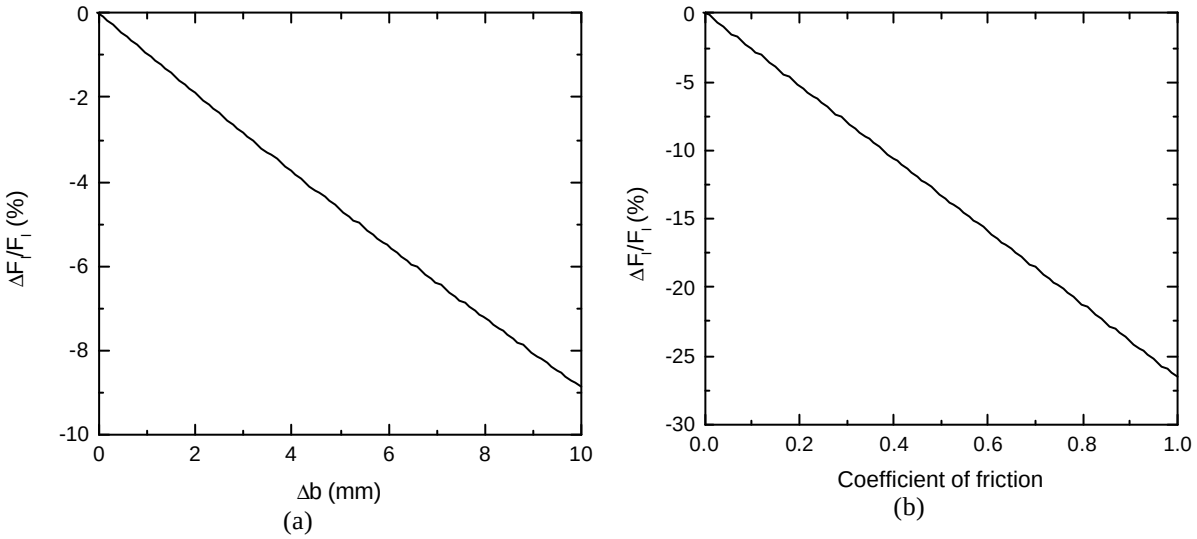

Figure 25 – Influence of the variation of the internal lever arm (a) and the value of the friction coefficient (b) on the relative variation of pullout force.

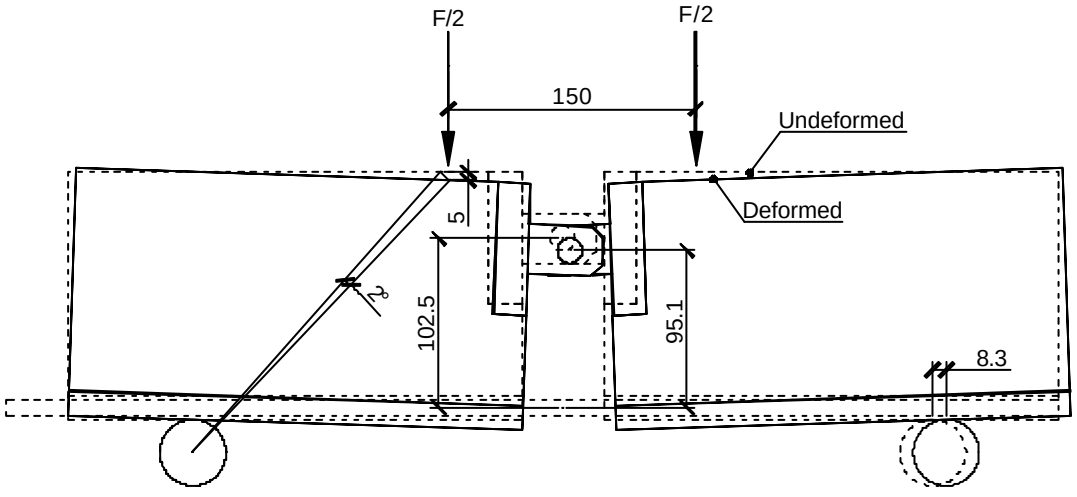

Figure 26 – Variation of the internal lever arm due the rigid body movement of the specimen.

Influence of the friction between the specimen and the loading system

To decrease the friction at the line interface between the loading steel devices and concrete, one layer of Teflon was interposed. The friction, however, was not fully eliminated, as Figure 27 shows, where a drop in the pullout force occurred when the resistance due to the friction was exceeded.

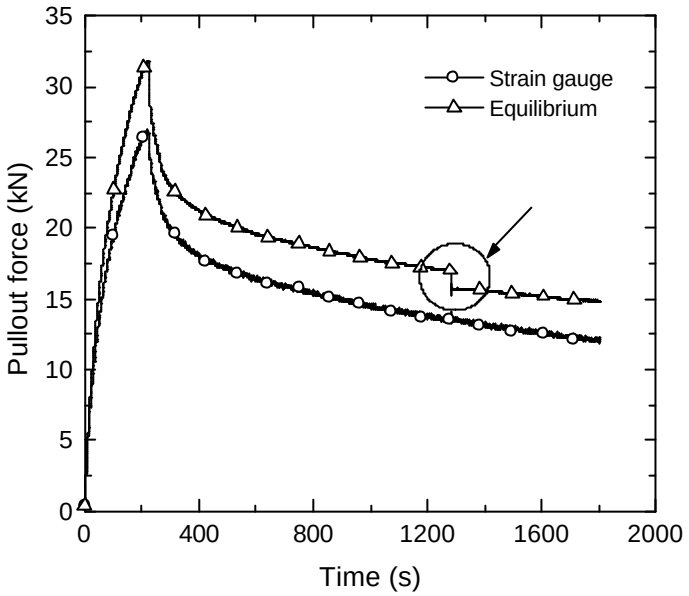

Figure 27 – Time evolution of the pullout force of the *B1_La120_M* specimen.

The influence of the friction between the concrete specimen and the load-applying system on the variation of the pullout force can be determined from the following expression:

$$\Delta F_l = -\frac{40j}{150} F_l \qquad \text{(Eq. 4)}$$

where j is the steel-concrete friction coefficient. The $\Delta F_l / F_l - j$ relationship is depicted in Figure 25(b) for distinct values of j. For example, ΔF_l is –5.3% of F_l is $j = 0.2$.

Amongst the factors that can justify the difference in the pullout force value obtained from strain gage and equilibrium, the most important are the variation of the internal lever arm and the existence of friction between the specimen and the loading system. Since the

strain gage approach is not influenced by the variation of the internal lever arm, the pullout force is calculated using the strain gage approach in following sections.

4.2.3 Slip at the free and loaded ends

Figure 28(a) depicts a typical time evolution of the slip measured at the free (LVDT1) and loaded (LVDT2) ends (see Figure 1). As expected, the slip at the loaded end has a linear evolution (slip measured by the controller LVDT2). The slip at the free end has a nonlinear time evolution. Appendix II includes the time evolution of the slips of all tested specimens.

Figure 28(b) shows a typical time evolution of the pullout force, the slip at the free and loaded ends. Analyzing the time evolution of the slip, the following four branches can be distinguished (Appendix II includes the graphs of all tested specimens):

- AB where slip occurs only at the loaded end;
- BC where slip occurs at the loaded and free ends. The free end slip up to point C, however, was negligible;
- CD where the slip rate at the free end is higher than the slip rate at loaded end;
- DE where slip rates are similar at both free and loaded ends.

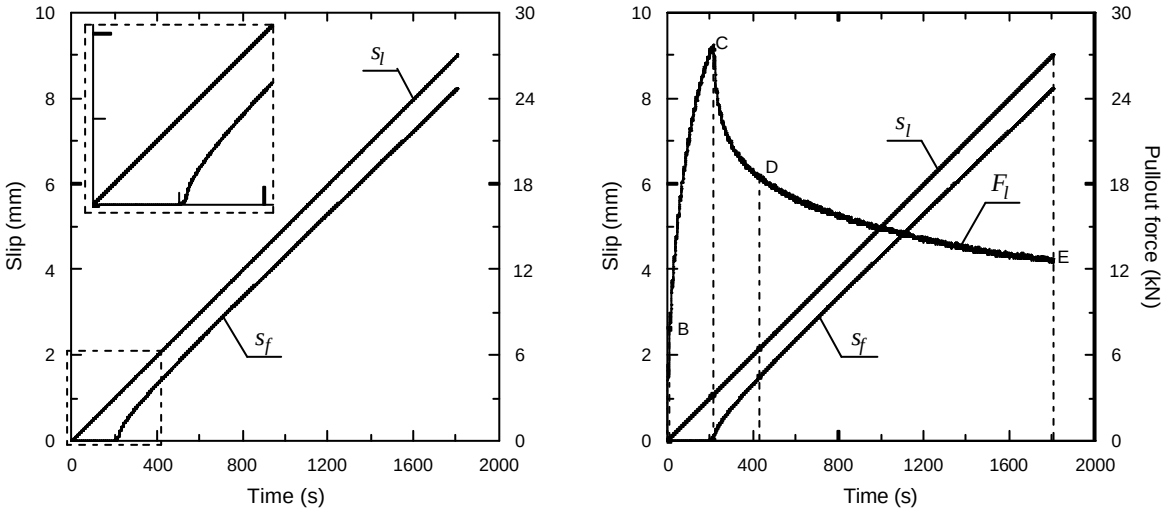

Figure 28 – Time evolution of the slip at free end (s_f) and loaded end (s_l) (a), and time evolution of the pullout force (F_l), slip at free end (s_f) and loaded end (s_l) (b), of the specimen *B3_Lb120_M*.

The physical interpretation of these four branches is described in detail elsewhere (Sena-Cruz and Barros 2002a, 2004). The values of the $F_l/F_{l\max}$ ratio for the points B, C and D were evaluated from the obtained experimental results, where F_l is the force at B, C or D points and $F_{l\max}$ is the maximum registered pullout force. These results are included in Table 10, from which it can be verified that: the force at point C is near the $F_{l\max}$ value; the forces at points B and D are about 20% and 65% of the $F_{l\max}$ value, respectively, but when compared to the values of $F_l/F_{l\max}$ at point C, a large scatter at points B and C was observed, mainly at point B. Along the bond length, homogeneity of the thickness and the physical properties of the epoxy adhesive are difficult to ensure. Furthermore, the behavior of the epoxy adhesive is perturbed by the presence of inevitable voids (Sena-Cruz et al. 2001). These factors influence the stress transfer between the laminate and the concrete and may have contributed to the scatter at points B and D.

Table 10 – Average values of the $F_l/F_{l\max}$ ratio for the points B, C and D.

Series	Ratio $F_l/F_{l\max}$		
	B	**C**	**D**
Lb60_M	0.180 (43.9%)	0.996 (0.5%)	0.598 (3.5%)
Lb90_M	0.246 (66.1%)	0.989 (0.5%)	0.654 (1.4%)
Lb120_M	0.229 (20.9%)	0.993 (0.5%)	0.669 (2.4%)

4.2.4 Pullout force *vs*. slip

Figure 29 to Figure 31 show the entire relationship between the pullout force and the slip at the free and loaded ends ($F_l - s_f$ and $F_l - s_l$) for the series of distinct bond length. Appendix II (from Figure II.13 to Figure II.15) includes the $F_l - s_l$ relationship up to $s_l = 2.0$ mm and the $F_l - s_f$ up to $s_f = 0.5$ mm. Analyzing $F_l - s_l$ and $F_l - s_f$ curves it is observed that, after a short linear branch, the response become nonlinear. The peak load has occurred at loaded end slip in the range of 0.38 mm to 1.24 mm. After sudden decay beyond the peak, the pullout force decreases smoothly with the increment of the slip, describing a nonlinear softening branch. The significant residual pullout force indicates that frictional mechanisms in concrete-adhesive-laminate interfaces are mobilized. Similar response was registered in all tested specimens.

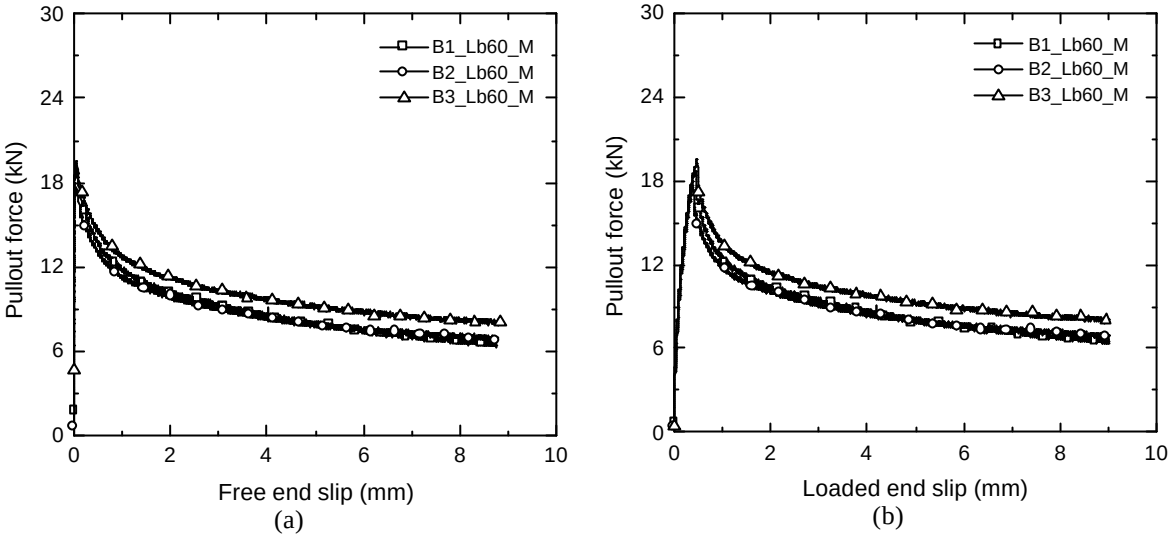

Figure 29 – Pullout load *vs*. free end slip (a) and *vs*. loaded end slip (b), of the series *Lb60_M*.

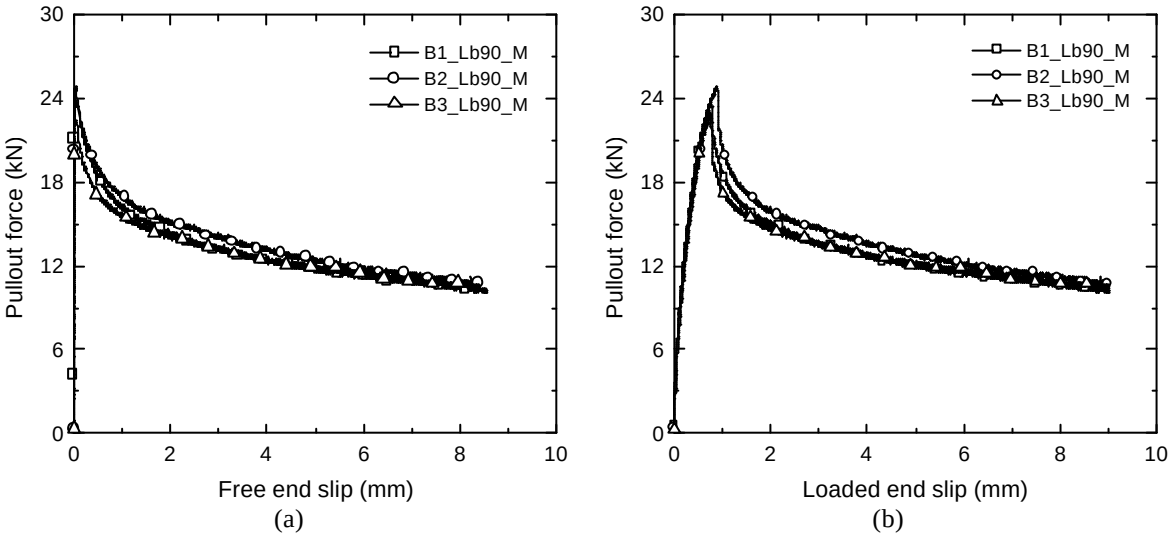

Figure 30 – Pullout load *vs*. free end slip (a) and *vs*. loaded end slip (b), of the series *Lb90_M*.

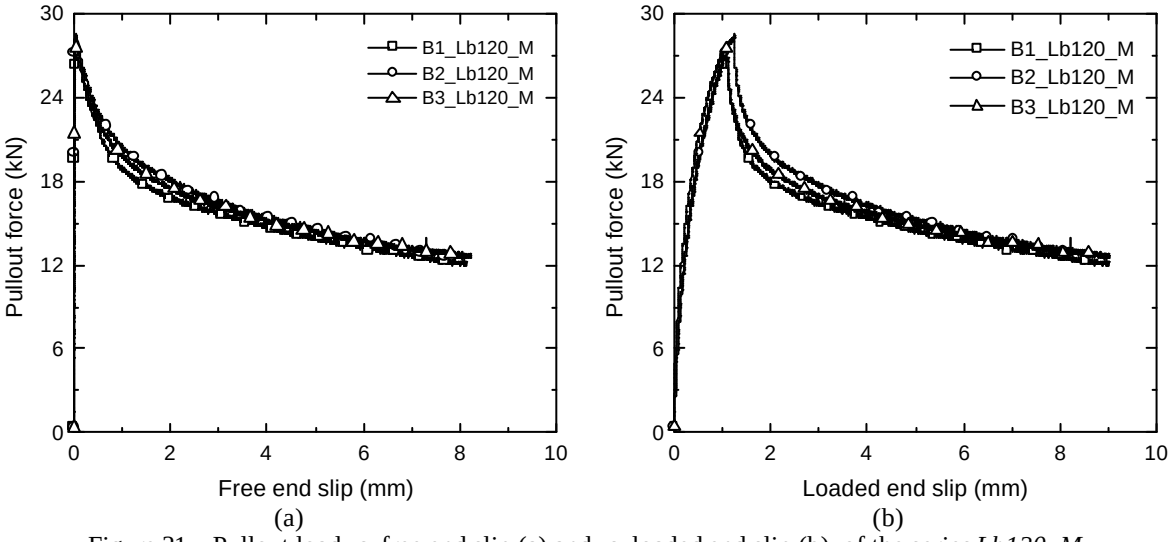

Figure 31 – Pullout load *vs*. free end slip (a) and *vs*. loaded end slip (b), of the series *Lb120_M*.

Analyzing $F_l - s_f$ curves it is observed that s_f at maximum pullout force is very small. After peak load, however, similar responses of $F_l - s_l$ and $F_l - s_f$ curves were recorded (see also Figure II.13(b) to Figure II.15(b)).

4.2.5 Bond stress *vs*. slip

Bond stress is obtained through dividing the pullout force, F_l, by the contact area between CFRP and epoxy adhesive, $F_l \Big/ \left(2\left(w_f + t_f\right)L_b\right)$, where w_f and t_f are the width and the thickness of the CFRP. Figure 32 to Figure 34 illustrate the relationship between the bond stress and the slip at the loaded and free ends for the series of distinct bond lengths.

4.2.6 Discussion of results

Table 11 includes the average values of the main parameters analyzed. In this table, $s_{f\max}$ and $s_{l\max}$ are the slip at the free and loaded ends at the peak pullout force ($F_{l\max}$), respectively. $t_{\max}$ is the average bond strength, defined according to previous paragraph replacing F_l by $F_{l\max}$. The expression $s_{l\max} / f_{fu}$ is the ratio between the CFRP stress at peak pullout force, $s_{l\max}$, and the CFRP tensile strength ($f_{fu} = 2800$ MPa). Finally, t_r is the residual bond stress, i.e., the bond stress at the end of the test (a loaded end slip of about 9.0 mm). The influence of the bond length on the main parameters analyzed is represented in Figure 35 to Figure 37.

The loaded end slip at the peak pullout force increases linearly with the bond length, L_b. The free end slip at peak pullout force was very small. The larger values of the coefficient of variation of $s_{f\max}$ are justified by the lack of precision of the LVDTs for measuring such small values.

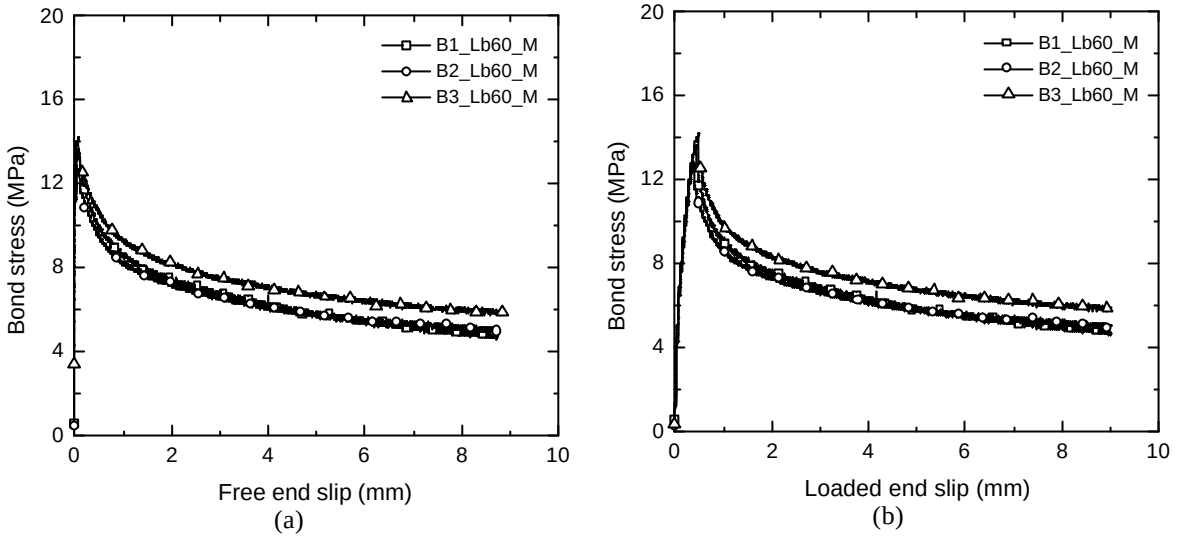

Figure 32 – Bond stress *vs*. free end slip (a) and *vs*. loaded end slip (b), of the series *Lb60_M*.

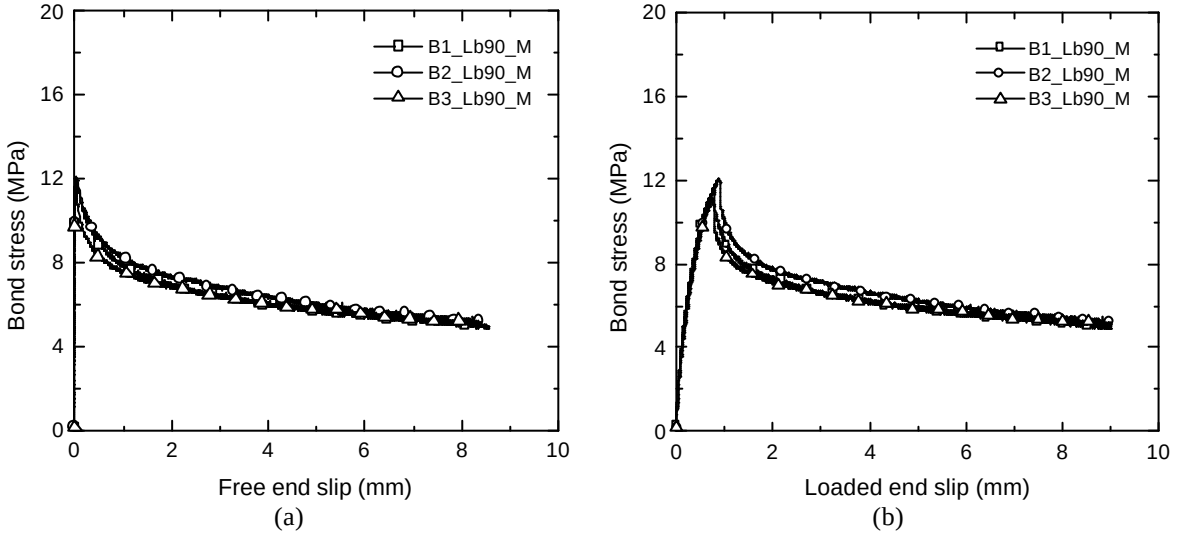

Figure 33 – Bond stress *vs*. free end slip (a) and *vs*. loaded end slip (b), of the series *Lb90_M*.

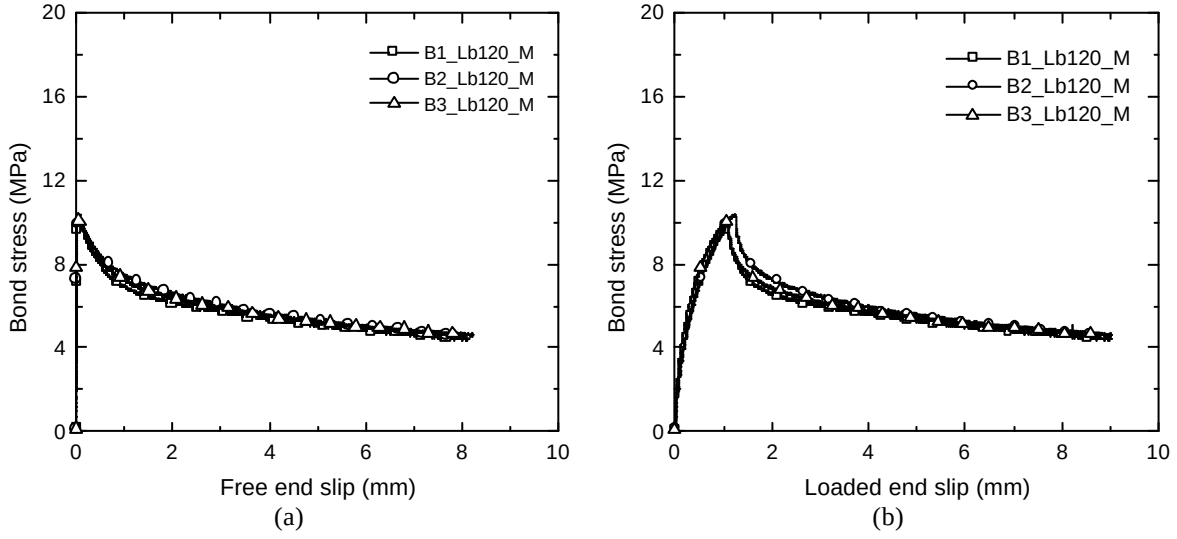

Figure 34 – Bond stress *vs*. free end slip (a) and *vs*. loaded end slip (b), of the series *Lb120_M*.

As already seen in previous research (Sena-Cruz and Barros 2002b), the peak pullout force increases with the bond length, but the increase rate decreases with the bond length. Applying an analytical model developed to simulate the bond behavior of the present strengthening technique (Sena-Cruz and Barros 2003), it was verified that at the peak pullout force the fraction of the bond length in the softening regime increases with the increase of the bond length. This indicates that the increase of the peak pullout force with the bond length would have an asymptote shape.

Similar behavior was observed for $s_{l\max}/f_{fu}$ and $t_r/t_{\max}$ ratios. Also, the bond strength decreases with the increase of the bond length.

Table 11 – Average values of the main parameters evaluated.

Series	$s_{f\max}$ (mm)	$s_{l\max}$ (mm)	$F_{l\max}$ (kN)	$t_{\max}$ (MPa)	$s_{l\max}/f_{fu}$ (%)	$t_r/t_{\max}$ (–)
Lb60_M	0.06 (19.83%)	0.43 (11.25%)	18.7 (5.1%)	13.6	47.5	0.39 (8.27%)
Lb90_M	0.03 (35.44%)	0.79 (9.02%)	23.9 (4.1%)	11.6	60.7	0.44 (4.36%)
Lb120_M	0.06 (22.01%)	1.13 (8.09%)	27.7 (2.8%)	10.1	70.5	0.45 (2.34%)

Note: the values in parentheses are the coefficients of variation of the corresponding series.

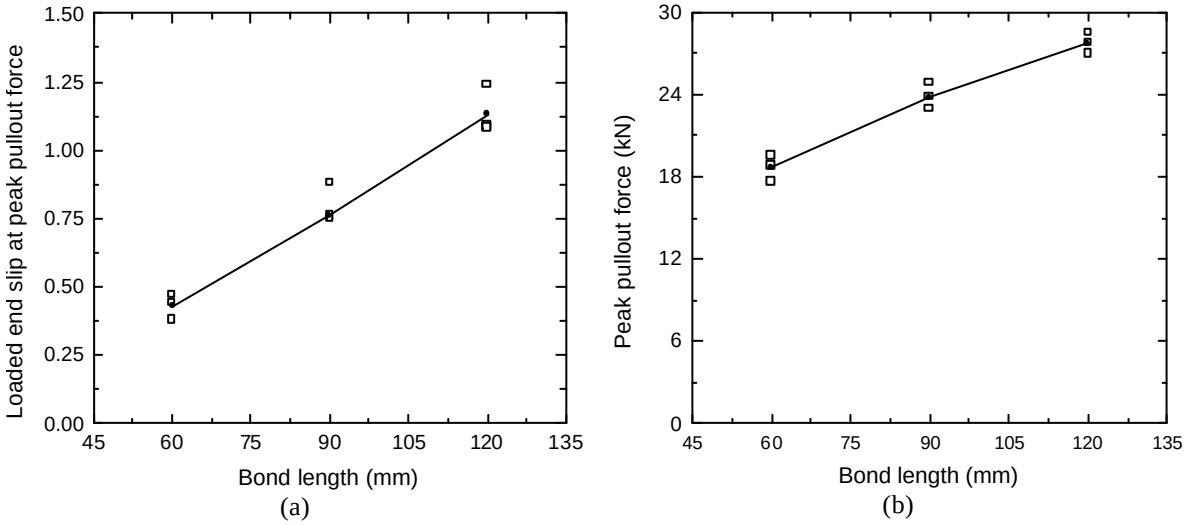

Figure 35 – Influence of the bond length on the loaded end slip at peak pullout force (a) and on the peak pullout force (b).

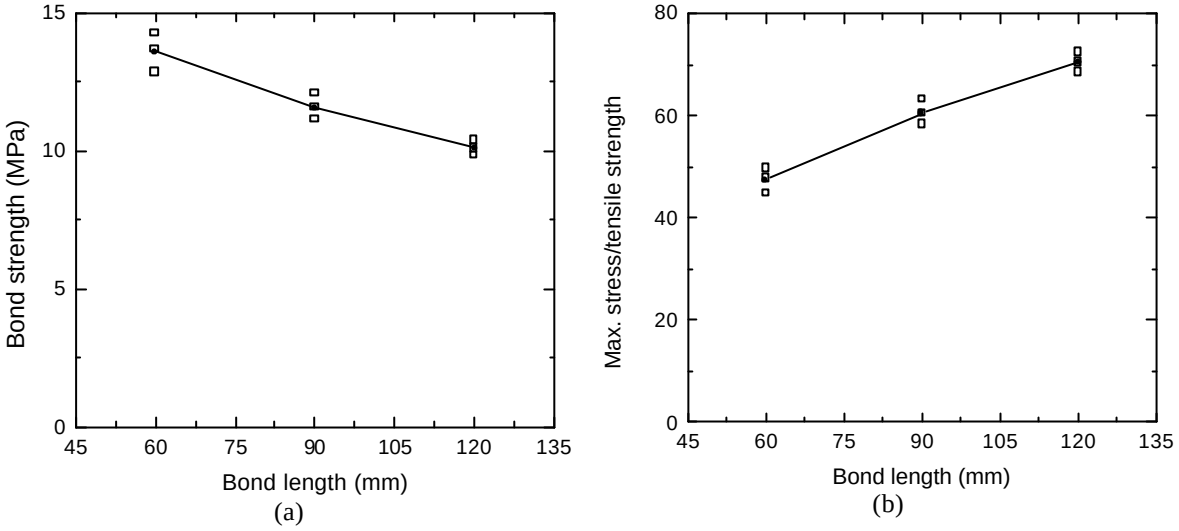

Figure 36 – Influence of the bond length on the bond strength (a) and on the ratio $s_{l\max}/f_{fu}$ (b).

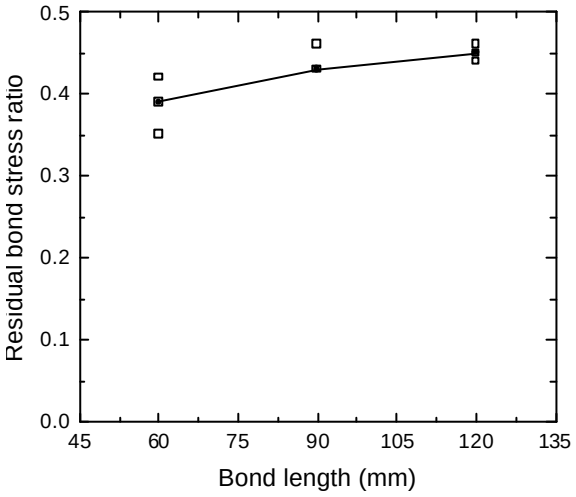

Figure 37 – Influence of the bond length on the ratio $t_r/t_{\max}$.

4.3 Cyclic loading results

4.3.1 Free end slip, loaded end slip and pullout force

Figure 38 and Figure 39 present the typical time evolution of the slip at free and loaded ends and the pullout force of the *C1* and *C10* series, respectively (Figure II.16 to include Figure II.27 all results). As these figures show, the free end slip has remained practically constant while the loaded end slip has decreased with a decrease in load in the unloading branches. In the loading/reloading branches, the slip at both the free and loaded ends has increased with the pullout force. The loaded end slip has a nonlinear time evolution in the unloading branches since these were performed under load control. Figure 39(b) shows

that the cycles at 75% of the bond strength before peak load have induced strength degradation in the bond.

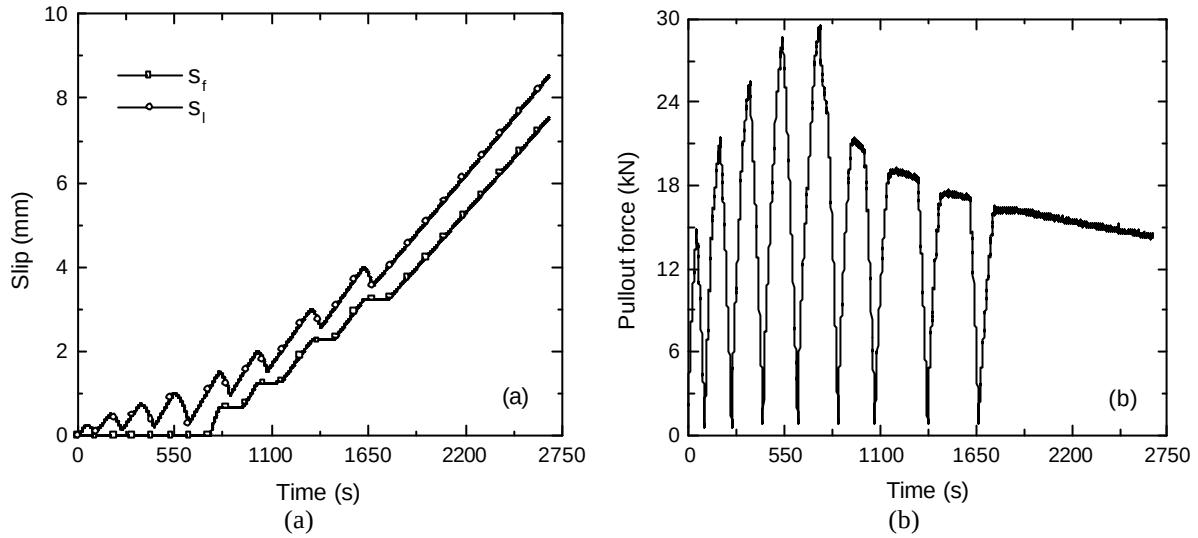

Figure 38 – Time evolution of the slip at free end (s_f) and loaded end (s_l) (a), and time evolution of the pullout force (F_l) of the specimen *B1_Lb120_C1*.

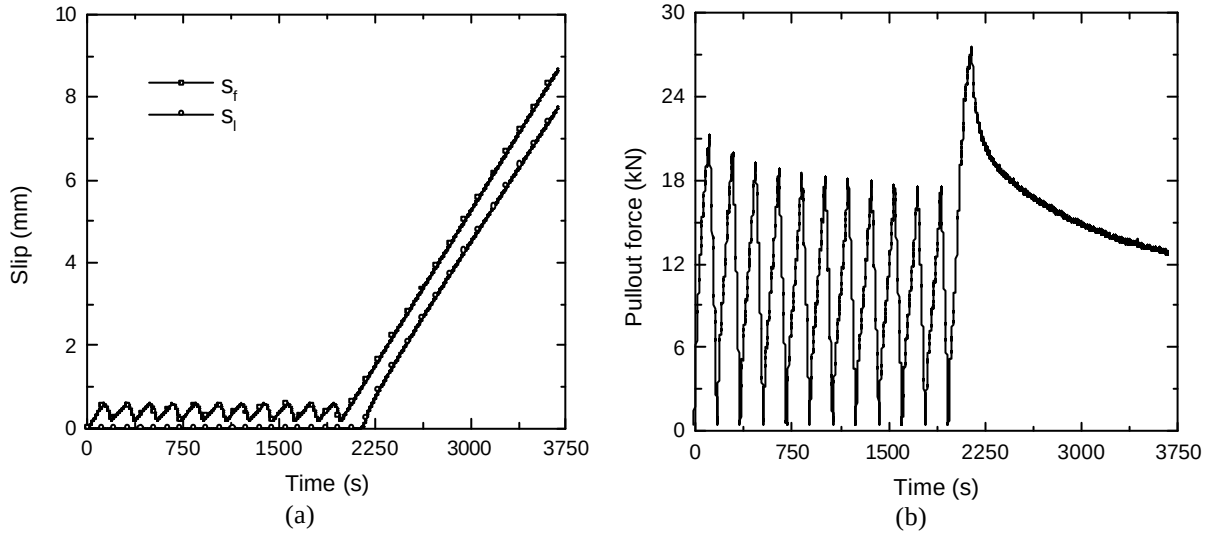

Figure 39 – Time evolution of the slip at free end (s_f) and loaded end (s_l) (a), and time evolution of the pullout force (F_l) of the specimen *B1_Lb120_C10*.

4.3.2 Pullout force *vs*. slip

Figure 40 and Figure 41 to Figure 43 show the entire relationships between the pullout force and the slip at the free and loaded ends ($F_l - s_f$ and $F_l - s_l$) for the series *C1* and

C10, respectively. Appendix II (from Figure II.28 to Figure II.31) includes the $F_l - s_f$ up to $s_f = 0.5\,\mathrm{mm}$ and the $F_l - s_l$ relationship up to $s_l = 1.0\,\mathrm{mm}$. For the series with equal bond length the monotonic curve was also included. This curve is the average response of the specimens composing this series.

These figures reveal that the envelope of the cyclic tests had a shape similar to the monotonic tests. The strength was affected marginally by the influence of the cyclic loading. Figure 40(a) indicates that the unloading/reloading cycles before peak load did not induce any free end slip.

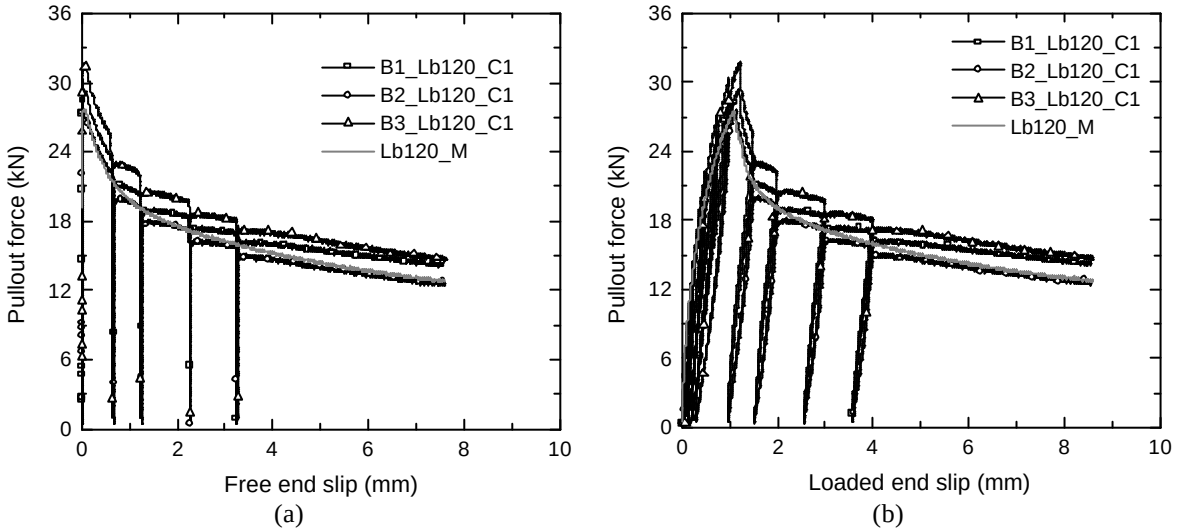

Figure 40 – Pullout load *vs*. free end slip (a) and *vs*. loaded end slip (b), of the series *Lb120_C1*.

4.3.3 Bond stress *vs*. slip

The bond stress *vs*. slip at the free and loaded end slips registered in the *C1* and *C10* series are depicted in Figure 44, and in Figure 45 to Figure 47, respectively. Appendix II includes these relationships up to a slip of practical interest (Figure II.32 to Figure II.35). The observations pointed out in $F_l - s_f$ and $F_l - s_l$ relations are applicable to the bond stress slip relationships also.

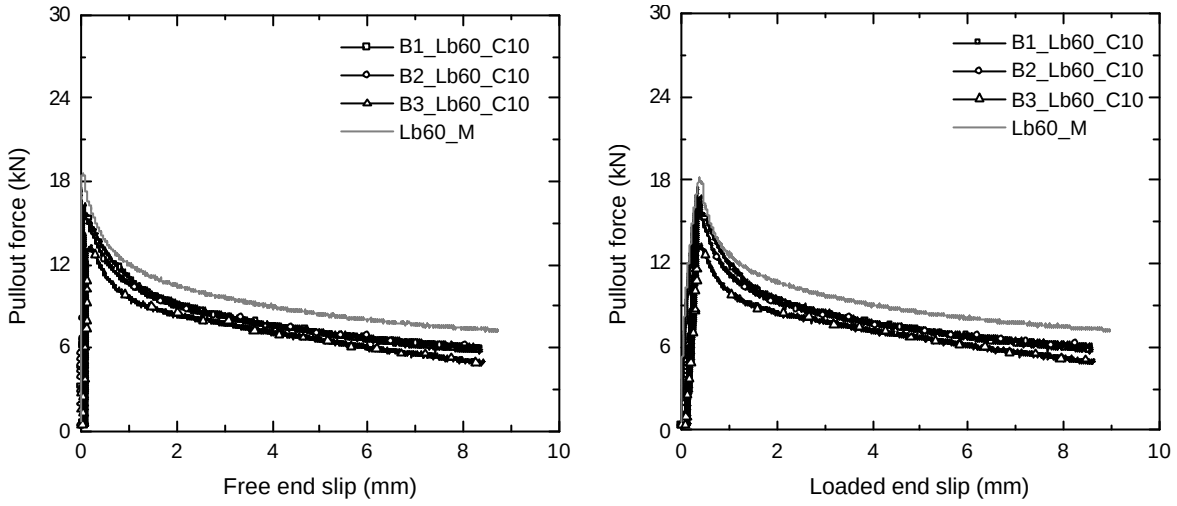

Figure 41 – Pullout load *vs*. free end slip (a) and *vs*. loaded end slip (b), of the series *Lb60_C10*.

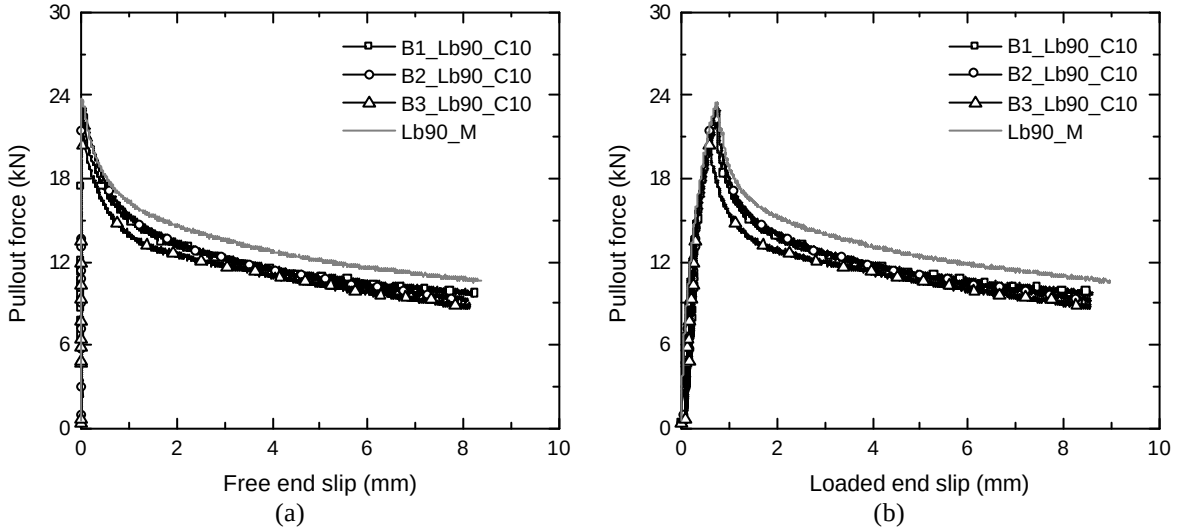

Figure 42 – Pullout load *vs*. free end slip (a) and *vs*. loaded end slip (b), of the series *Lb90_C10*.

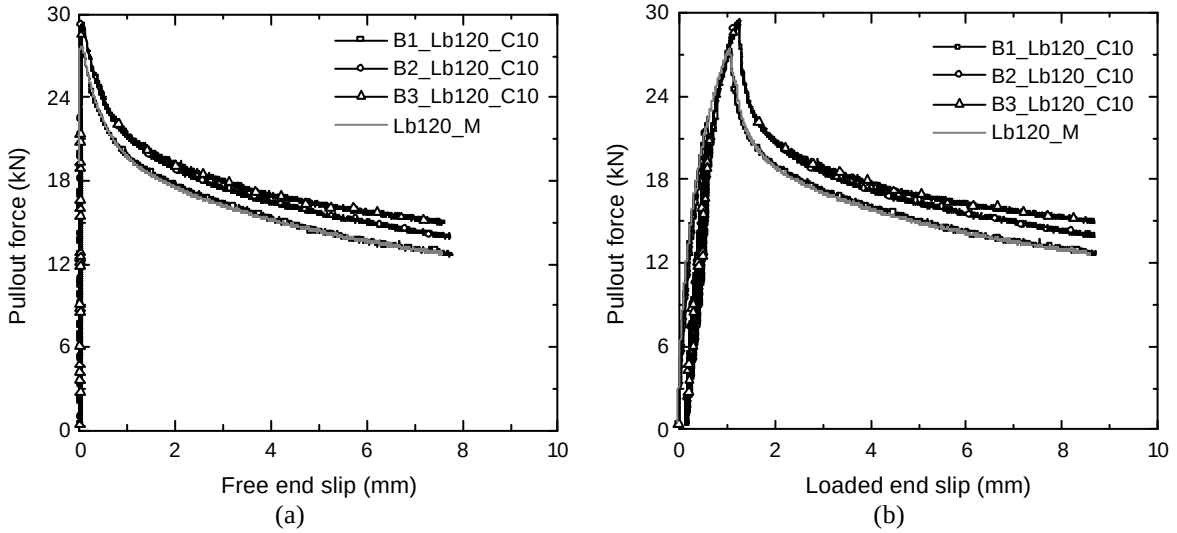

Figure 43 – Pullout load *vs*. free end slip (a) and *vs*. loaded end slip (b), of the series *Lb120_C10*.

4.3.4 Discussion of results

Table 12 includes the average values of the main parameters analyzed. Comparing these values to those obtained in the homologous monotonic series, the former are smaller, in general. Series *Lb120* was the only exception to this tendency, and no clear justification can be made for this behavior.

An example of the influence of the loading cycles on the stiffness degradation evolution of the *C1* series is presented in the Figure 48(a). This stiffness was defined as the slope of the line connecting the points (circles in Figure 48(a)) corresponding to unloading and reloading initiation.

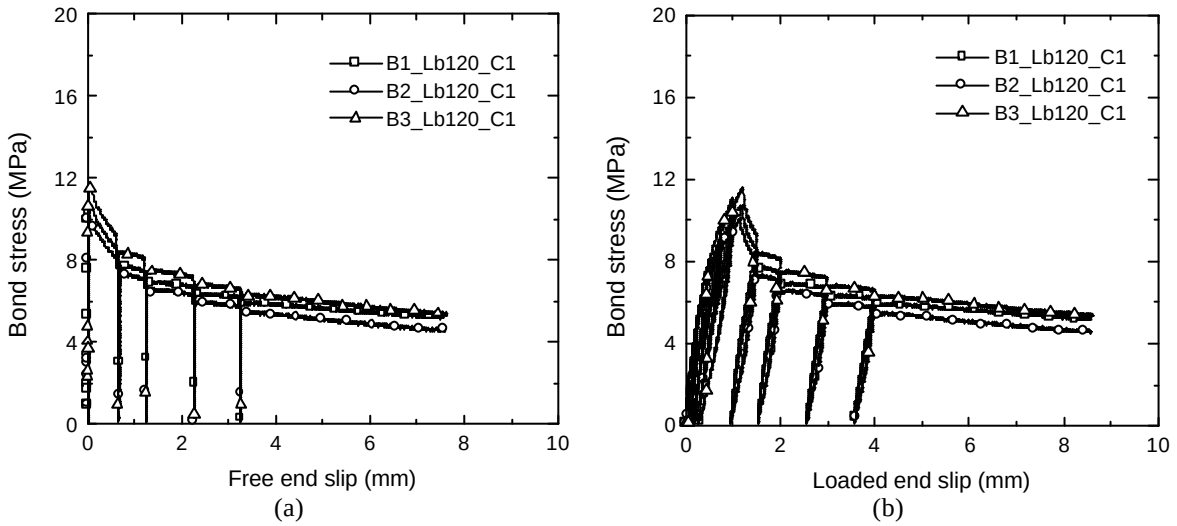

Figure 44 – Bond stress *vs*. free end slip (a) and *vs*. loaded end slip (b), of the series *Lb120_C1*.

Table 12 – Average values of the main parameters evaluated.

Series	$s_{f\max}$ (mm)	$s_{l\max}$ (mm)	$F_{l\max}$ (kN)	$t_{\max}$ (MPa)	$s_{l\max}/f_{fu}$ (%)	$t_r/t_{\max}$ (–)
Lb120_C1	0.05 (32.79%)	1.18 (2.81%)	29.6 (6.9%)	10.8 (6.9%)	75.53 (6.89%)	0.47 (4.33%)
Lb60_C10	0.03 (90.41%)	0.35 (13.43%)	16.6 (5.2%)	12.1 (5.2%)	42.22 (5.19%)	0.33 (8.10%)
Lb90_C10	0.04 (40.05%)	0.69 (11.96%)	22.2 (4.7%)	10.8 (4.7%)	56.35 (4.67%)	0.42 (5.25%)
Lb120_C10	0.04 (7.56%)	1.20 (8.36%)	28.8 (4.1%)	10.5 (4.1%)	73.15 (4.09%)	0.48 (4.74%)

Note: the values in parentheses are the coefficients of variation of the corresponding series.

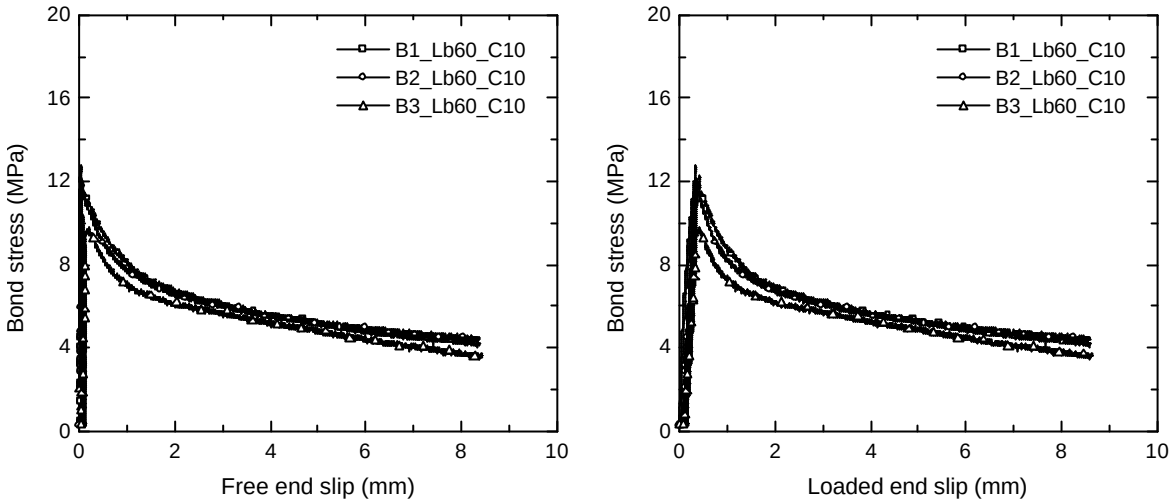

Figure 45 – Bond stress *vs*. free end slip (a) and *vs*. loaded end slip (b), of the series *Lb60_C10*.

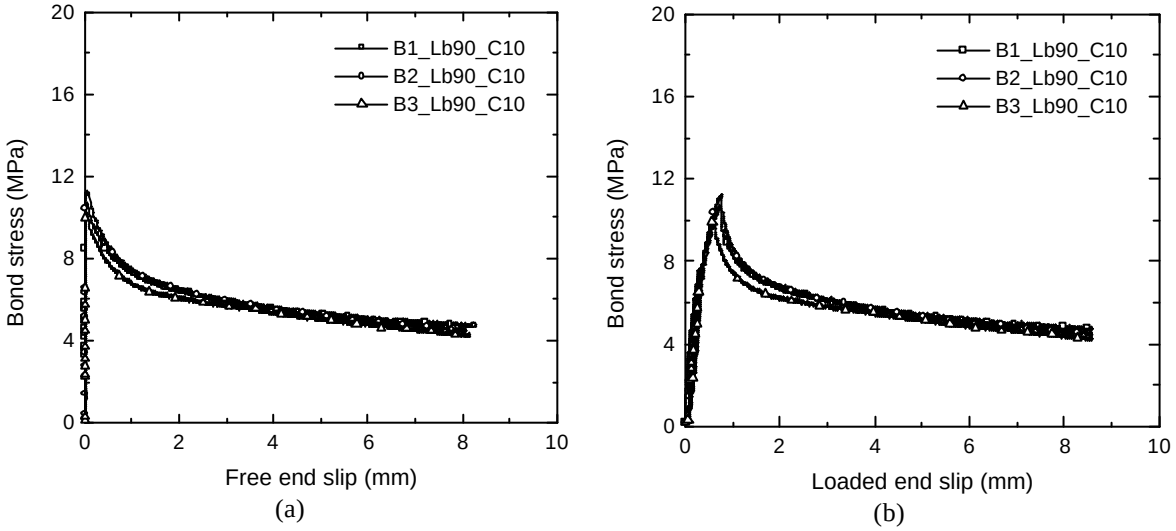

Figure 46 – Bond stress *vs*. free end slip (a) and *vs*. loaded end slip (b), of the series *Lb90_C10*.

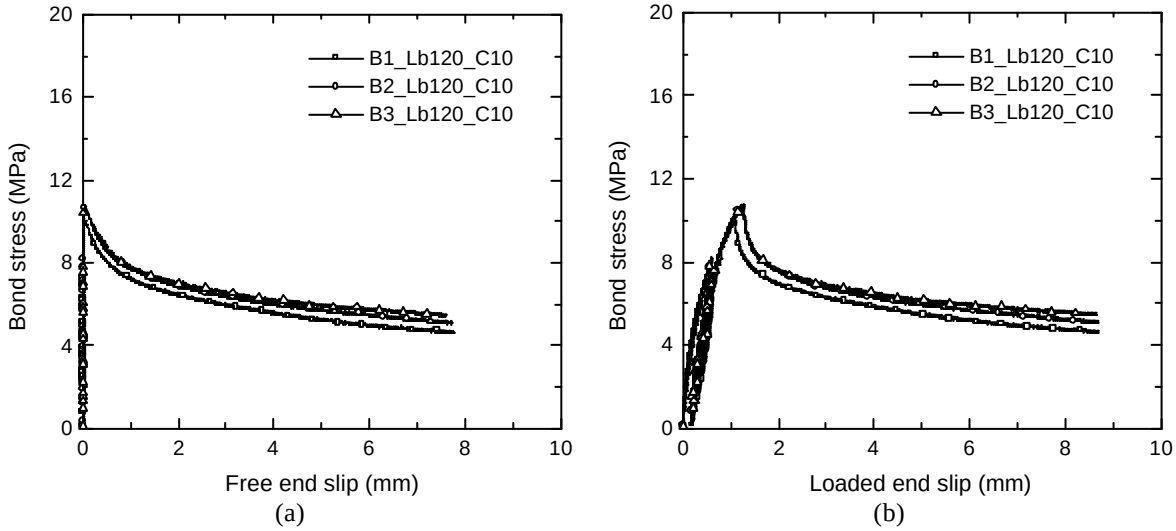

Figure 47 – Bond stress *vs*. free end slip (a) and *vs*. loaded end slip (b), of the series *Lb120_C10*.

Figure 48(b) represents the stiffness variation with the loaded end slip of the *Lb120_C1* series. This chart shows that up to the peak pullout force the stiffness decreases significantly, while in the first phase of the softening branch a slight increase was registered, followed by a reduced decrease. The mechanisms involved in the pre- and post-peak pullout force dictates this distinct behavior. Up to the peak pullout force, significant CFRP-adhesive and adhesive-concrete debonding occurs, along with adhesive cracking, leading to a significant decrease of the bond stiffness. In the post-peak regime, the sudden decay of the pullout force induces a typical increase of stiffness that occurs when the materials are submitted to large instantaneous load or displacement variations. When this phase stabilizes the bond stiffness is governed by the friction between the failing surfaces in the bond length, which decreases smoothly as slip increases.

Figure 49 includes the normalized pullout force as function of the number of cycles of the *C10* series. The normalized pullout force was defined, for each specimen, as the ratio between the maximum pullout force of the reloading branch of the cycle in analysis and the test peak pullout force. This chart reveals that the influence of the load cycles on the strength degradation was similar in all series, with an average strength degradation of 17%.

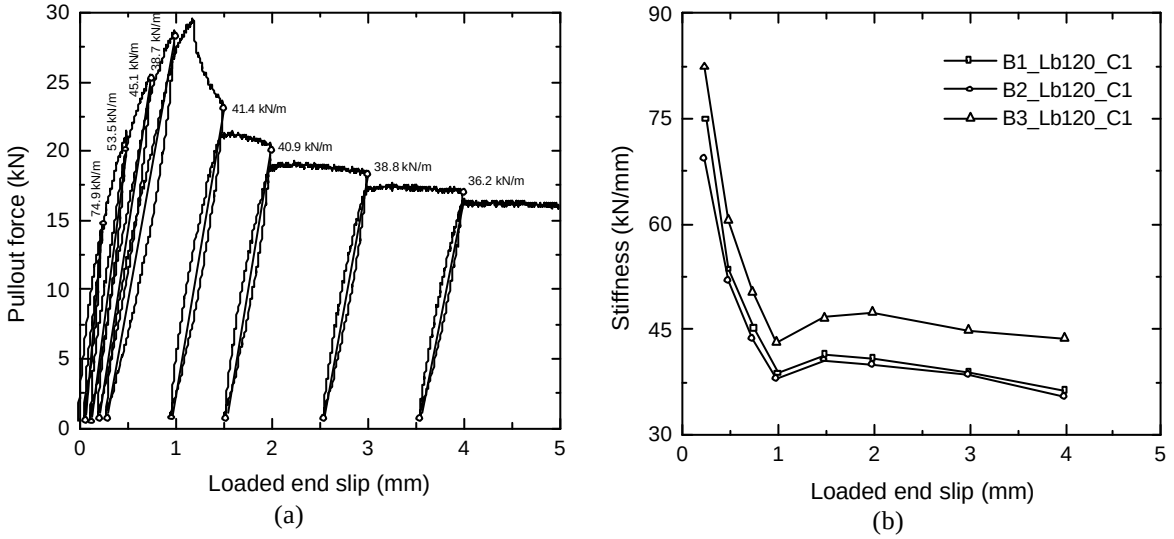

Figure 48 – Stiffness degradation evolution of the specimen B1_Lb120_C1 (a) and the Lb120 series (b).

After the fifth cycle, a larger degradation occurred in the specimen B3_Lb60_C10, since these cycles were performed in the post-peak regime, while in the remaining specimens all cycles were executed before the peak.

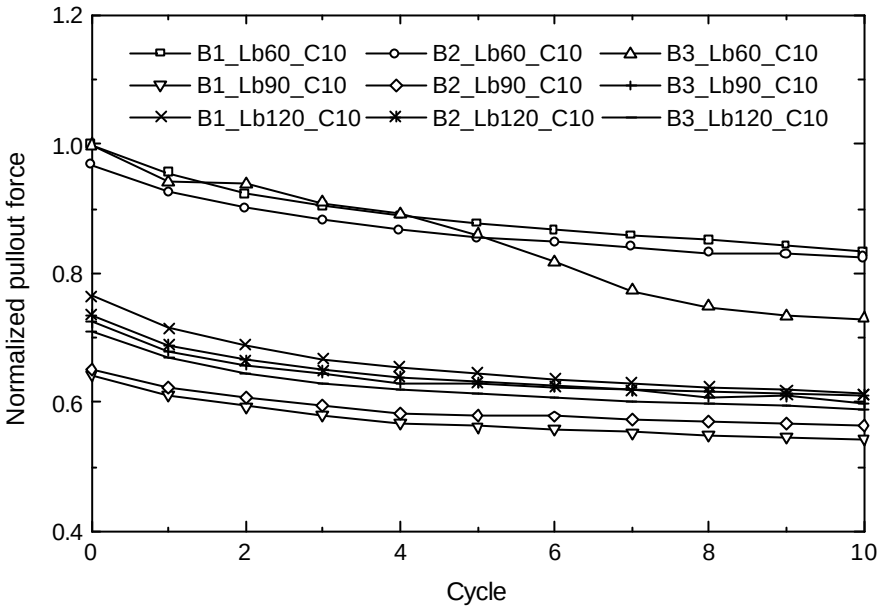

Figure 49 – Normalized pullout force as a function of the number of cycles.

5 CONCLUSIONS

To assess the bond performance of laminate strips of Carbon Fiber Reinforced Polymer (CFRP) to concrete under monotonic and cyclic loading, pullout-bending tests were carried out. The influence of the bonded length (Lb) and the load history were analyzed through tests with Lb=60, 90 and 120 mm and through monotonic tests (M) and cyclic tests (C1 - one cycle of loading/unloading at different slip levels; C10 - ten cycles of loading/unloading at a fixed load level). From the results obtained in the experimental program, the following conclusions can be pointed out:

1. The nonlinear branch before the peak in the pullout force increased with Lb;
2. The peak pullout force increased with Lb;
3. The bond strength ranges from 10 MPa to 14 MPa, with a tendency to decrease with an increase of Lb;
4. The ratio between the maximum tensile stress in the CFRP laminate and its tensile strength increased with Lb;
5. The loaded end slip at peak pullout force showed a linearly increasing trend with Lb;

6. The envelop of the pullout force-slip relationship in the cyclic tests was similar to the curve obtained in the corresponding monotonic tests;
7. A continuous decrease of the peak pullout force was observed in the unloading/reloading cycles before peak pullout force. The peak pullout force, however, was not affected by this effect;
8. In the unloading branches of the loading cycles performed in the post-peak regime, no slip at the free end was recovered;
9. The stiffness (i.e., average cyclic inclination) up to the peak pullout force was affected by the cycle loading, with a significant decrease. At the initiation of the softening phase the stiffness increased slightly, followed by a smooth decrease.

6 ACKNOWLEDGEMENTS

The first author of the present report would like to thank of Prof. Joaquim Barros and Dr. Ravindra Gettu, the supervisors of this work. He would like to thank to Prof. Joaquim Barros for his carefully advice, suggestions and incitement along the research. He thanks Dr. Ravindra Gettu for his interest, suggestions, care and for making his stay at Universitat Politecnica de Catalunya possible.

The help of Miguel Angel Martín and Ernesto Diaz, and the other technicians of the Structural Technology Laboratory during the experimental work is gratefully appreciated.

The first author wishes to acknowledge the grant SFRH/BD/3259/2000 provided by FCT and FSE. The tests at the Universitat Politecnica de Catalunya were partially supported by the Spanish Ministry of Science and Technology grant PB98-0293.

The authors would like to thank the Bettor MBT®, Spain, and Carles Cots, in particular, for providing the adhesive, as well as to S&P® for providing the laminates.

7 REFERENCES

Barros, J.A.O., and Fortes, A.S. (2002). "Concrete beams reinforced with carbon laminates bonded into slits." *Proc., 5th Congreso de Métodos Numéricos en Ingeniería* (CD-ROM), Madrid, Spain.

Barros, J.A.O., and Dias, S.J.E. (2003). "Shear strengthening of reinforced concrete beams with laminate strips of CFRP." *Proc., International Conference of Composites in Construction*, D. Bruno, G. Spadea and N. Swamy, eds., Cosenza, Italy, 289-294.

Bettor MBT (1999), "Mbrace Laminado", *Technical sheet*, Barcelona, Spain, June, 2 pp.

DARACEM® (2001), <http://www.na.graceconstruction.com/> (2003-02-05).

Ferreira, D.R.S.M. (2000). "Pilares de Betão Armado Reforçados com Laminados de Fibras de Carbono (Reinforced concrete columns strengthened with CFRP laminates)." *MSc Thesis*, Civil Eng. Dep., University of Minho, Portugal (in Portuguese).

ISO 527-5 (1997). "Plastics – Determination of tensile properties – Part 5: Test conditions for unidirectional fibre-reinforced plastic composites." *International Organization for Standardization*, Genève, Switzerland, 9 pp.

NP 196-1 (1990). "Métodos de ensaio de cimentos." *Instituto Português da Qualidade*, Lisbon, June, 29 pp.

RILEM (1982). "Bond test for reinforcement steel. 1. Beam test." TC9-RC.

Sena-Cruz, J.M.S., Barros, J.A.O., and Faria, R.M.C.M. (2001). "Assessing the embedded length of epoxy bonded carbon laminates by pull-out bending tests." *Proc., International Conference Composites in Construction*, Figueiras, J., Juvandes, L., and Faria, R., eds., Porto, Portugal, 217-222.

Sena-Cruz, J.M., and Barros, J.A.O. (2002a). "Caracterização experimental da ligação de laminados de CFRP inseridos no betão de recobrimento (Experimental characterization of CFRP laminates bonded to concrete cover)." *Rep. No 02-DEC/E-15*, Dept. of Civil Engrg., University of Minho, pp. 54 (in Portuguese).

Sena-Cruz, J.M., and Barros, J.A.O. (2002b). "Bond behavior of carbon laminate strips into concrete by pullout-bending tests." *Proc., Bond in Concrete – from the research to standards, International Symposium*, G. Balazs, P. Bartos, J. Cairns and A. Borosnyoi, eds., 20-22 November, Budapest, Hungry, 614-621.

Sena-Cruz, J.M., and Barros, J.A.O. (2003). "Bond between near-surface mounted CFRP laminates and the concrete in structural strengthening." *Proc., International Conference of Composites in Construction*, D. Bruno, G. Spadea and N. Swamy, eds., Cosenza, Italy, 397-402.

Sena-Cruz, J.M., and Barros, J.A.O. (2004). "Bond between near-surface mounted CFRP laminate strips and concrete." *J. Compos. for Const., ASCE* (to be published).

APPENDIX I

Table I.1 – Dimensions of the groove in the test region.

Specimen	Width (mm)		Depth (mm)	
	Free end	Loaded end	Free end	Loaded end
B1_Lb60_M	4.75	4.75	14.93	14.76
B2_Lb60_M	4.71	4.70	15.29	15.20
B3_Lb60_M	4.53	4.60	14.54	14.17
B1_Lb90_M	4.88	4.79	15.09	14.70
B2_Lb90_M	4.91	4.85	15.18	14.92
B3_Lb90_M	4.69	4.78	14.55	14.36
B1_Lb120_M	4.96	5.04	15.27	14.41
B2_L1b20_M	4.70	4.73	14.05	14.22
B3_Lb120_M	4.42	4.71	14.90	14.33
B1_Lb120_C1	4.88	4.94	15.36	14.81
B2_Lb120_C2	4.67	4.69	15.26	14.64
B3_Lb120_C2	4.66	4.60	14.22	15.02
B1_Lb60_C10	4.58	4.91	14.54	14.68
B2_Lb60_C10	4.88	5.02	14.49	14.29
B3_Lb60_C10	4.96	4.97	14.52	14.58
B1_Lb90_C10	5.19	5.16	14.70	14.71
B2_Lb90_C10	5.02	5.04	14.57	14.44
B3_Lb90_C10	4.81	4.62	15.25	14.87
B1_Lb120_C10	4.73	4.90	14.88	14.59
B2_Lb120_C10	4.77	4.89	14.88	14.22
B3_Lb120_C10	4.97	4.90	14.67	14.34

APPENDIX II

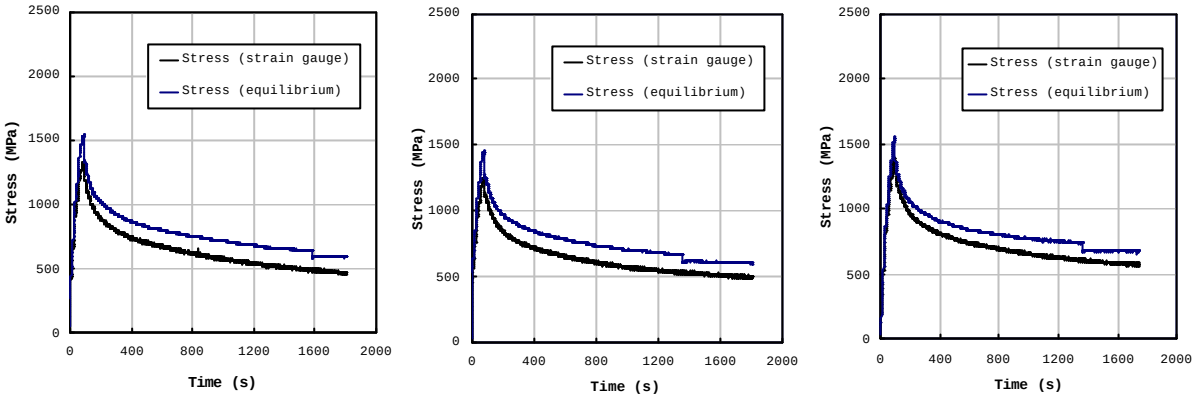

(a) (b) (c)

Figure II.1 – Time evolution of stress at the CFRP laminate of the specimens *B1_Lb60_M* (a), *B2_Lb60_M* (b) and *B3_Lb60_M* (c).

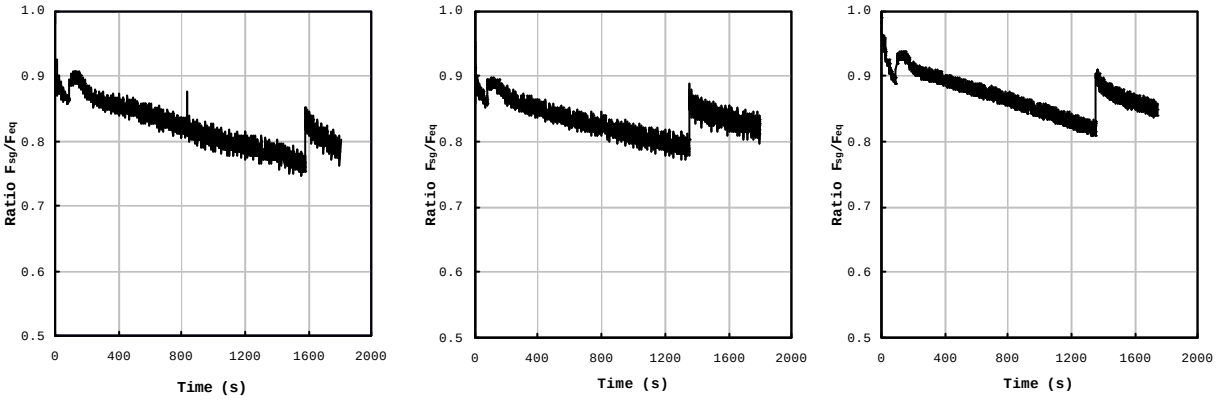

(a) (b) (c)

Figure II.2 – Time evolution of ratio F_{sg}/F_{eq} of the specimens *B1_Lb60_M* (a), *B2_Lb60_M* (b) and *B3_Lb60_M* (c).

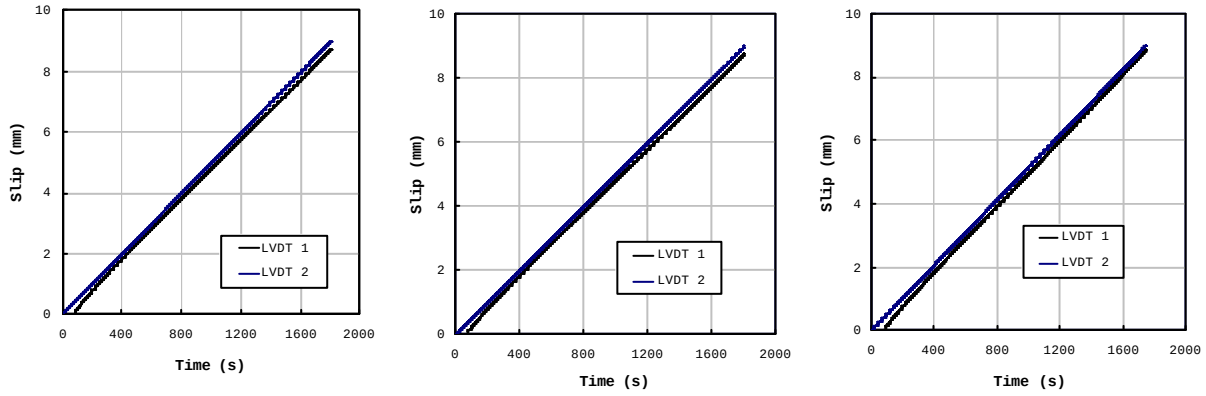

(a) (b) (c)

Figure II.3 – Time evolution of free end and loaded end slips of the specimens *B1_Lb60_M* (a), *B2_Lb60_M* (b) and *B3_Lb60_M* (c).

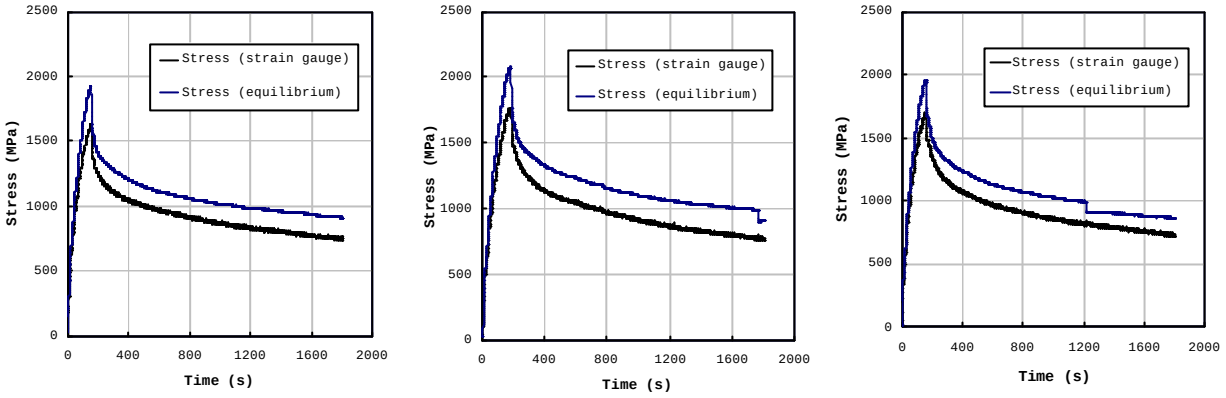

(a) (b) (c)

Figure II.4 – Time evolution of stress at the CFRP laminate of the specimens *B1_Lb90_M* (a), *B2_Lb90_M* (b) and *B3_Lb90_M* (c).

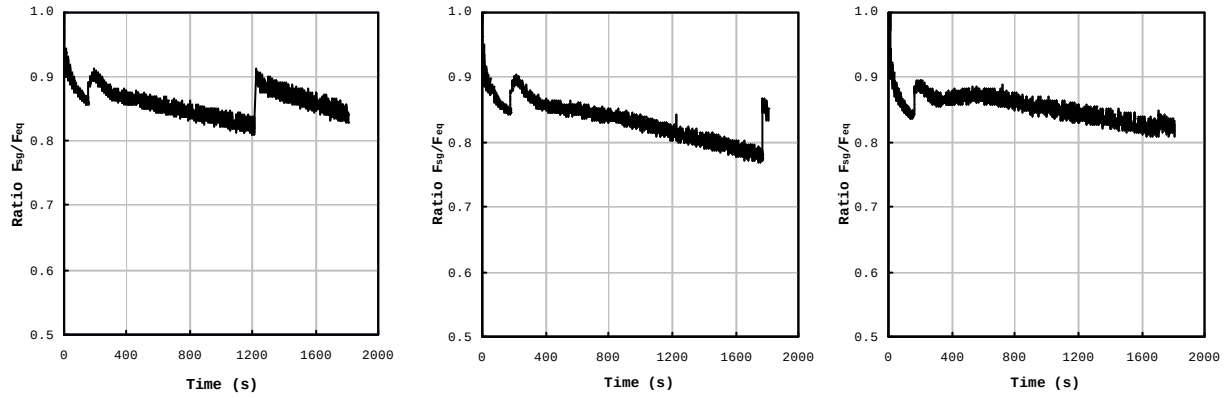

(a) (b) (c)

Figure II.5 – Time evolution of ratio F_{sg}/F_{eq} of the specimens *B1_Lb90_M* (a), *B2_Lb90_M* (b) and *B3_Lb90_M* (c).

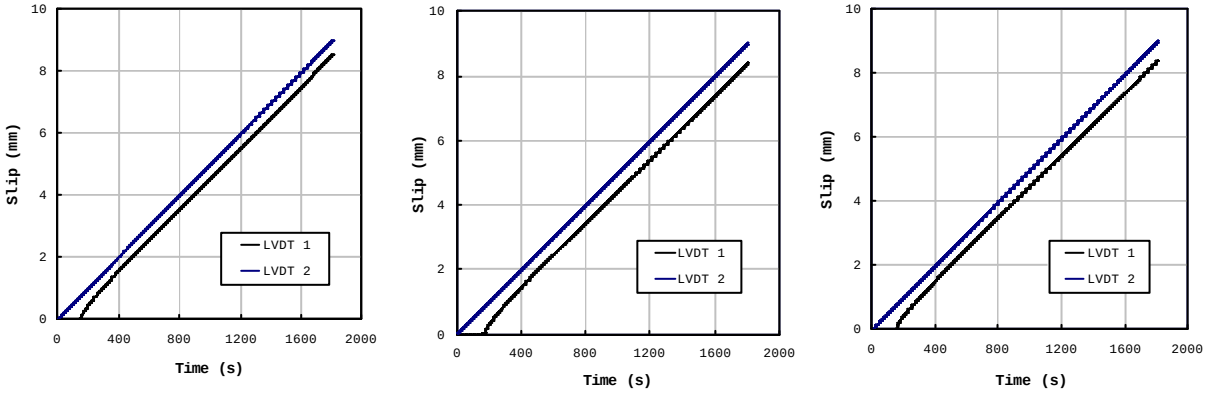

(a) (b) (c)

Figure II.6 – Time evolution of free end and loaded end slips of the specimens *B1_Lb90_M* (a), *B2_Lb90_M* (b) and *B3_Lb90_M* (c).

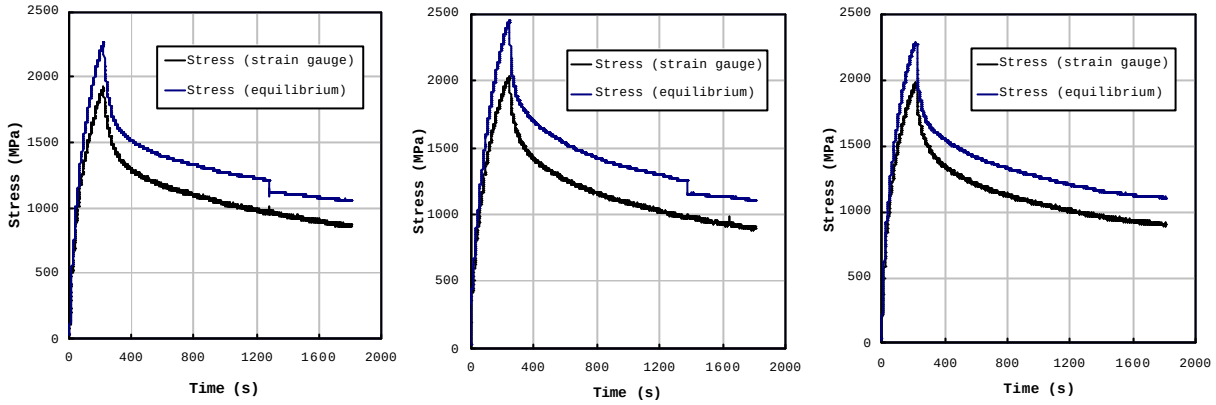

(a) (b) (c)

Figure II.7 – Time evolution of stress at the CFRP laminate of the specimens *B1_Lb120_M* (a), *B2_Lb120_M* (b) and *B3_Lb120_M* (c).

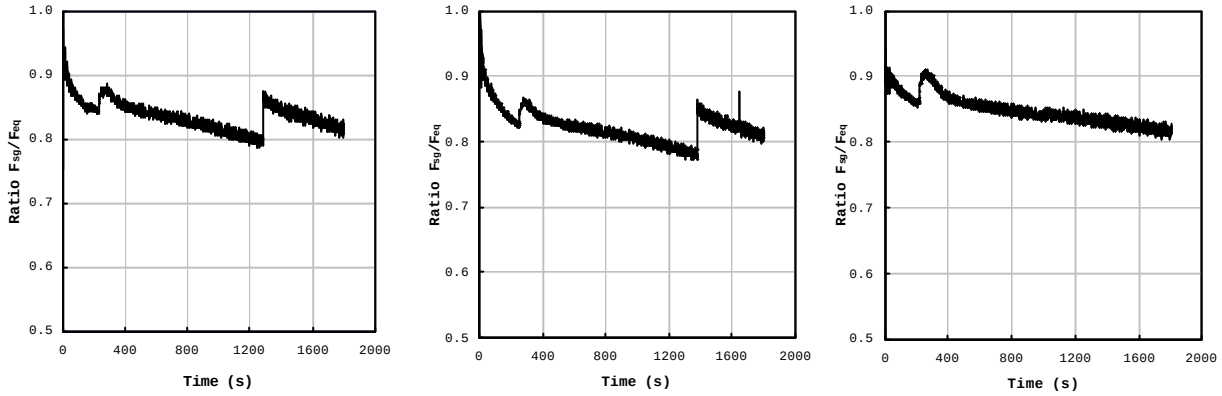

(a) (b) (c)

Figure II.8 – Time evolution of ratio F_{sg}/F_{eq} of the specimens *B1_Lb120_M* (a), *B2_Lb120_M* (b) and *B3_Lb120_M* (c).

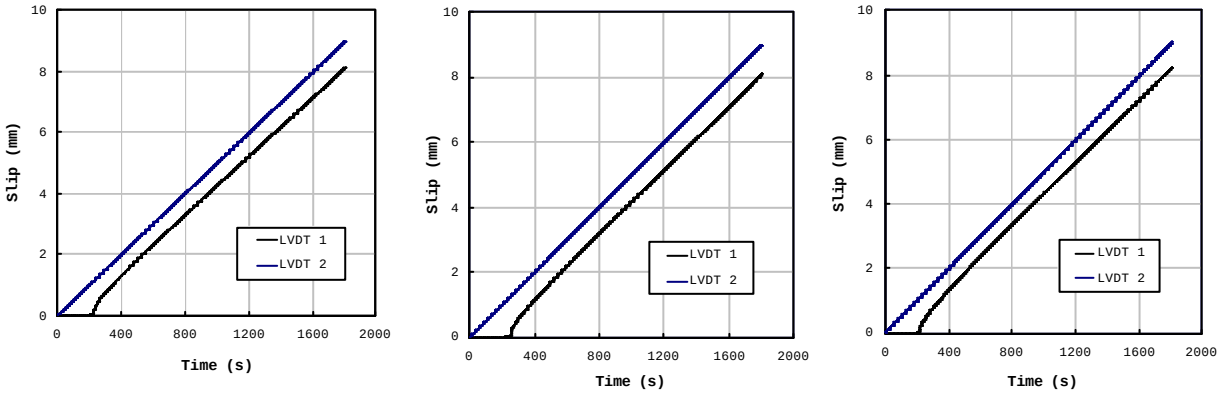

(a) (b) (c)

Figure II.9 – Time evolution of free end and loaded end slips of the specimens *B1_Lb120_M* (a), *B2_Lb120_M* (b) and *B3_Lb120_M* (c).

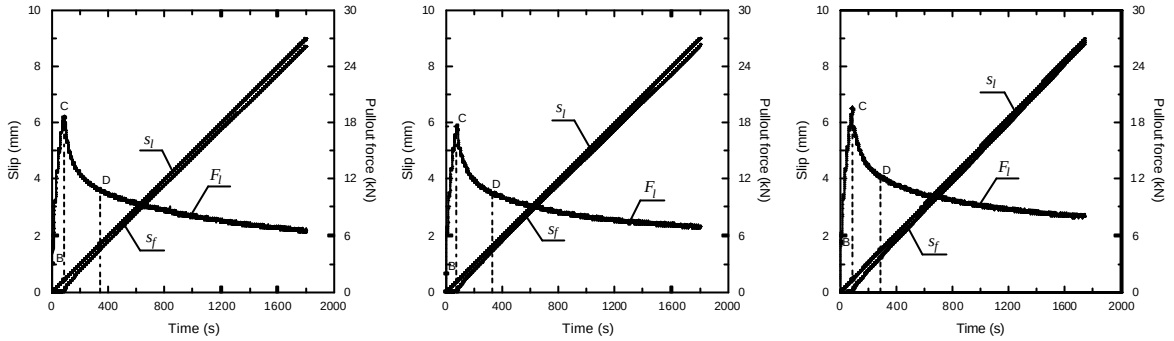

(a) (b) (c)

Figure II.10 – Time evolution of pullout force (F_l), and the slip at free end (s_f) and loaded end (s_l), of the specimen *B1_La60_M* (a), *B2_La60_M* (b) and *B3_La60_M* (c).

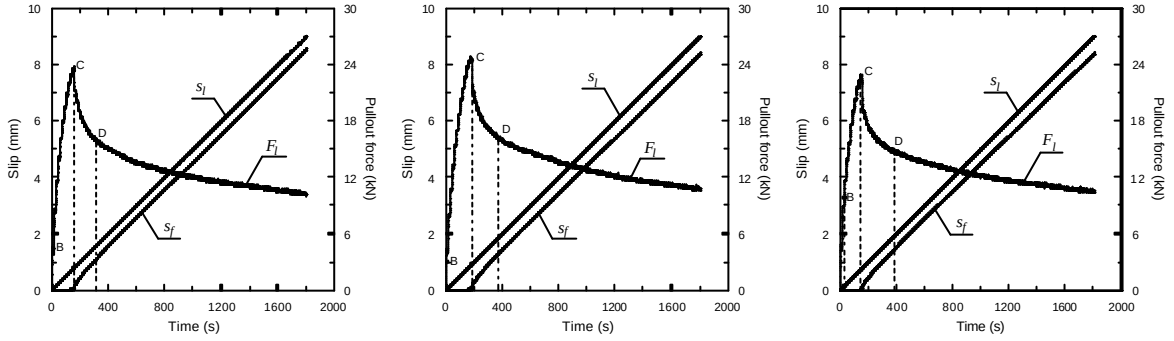

(a) (b) (c)

Figure II.11 – Time evolution of pullout force (F_l), and the slip at free end (s_f) and loaded end (s_l), of the specimen *B1_La90_M* (a), *B2_La90_M* (b) and *B3_La90_M* (c).

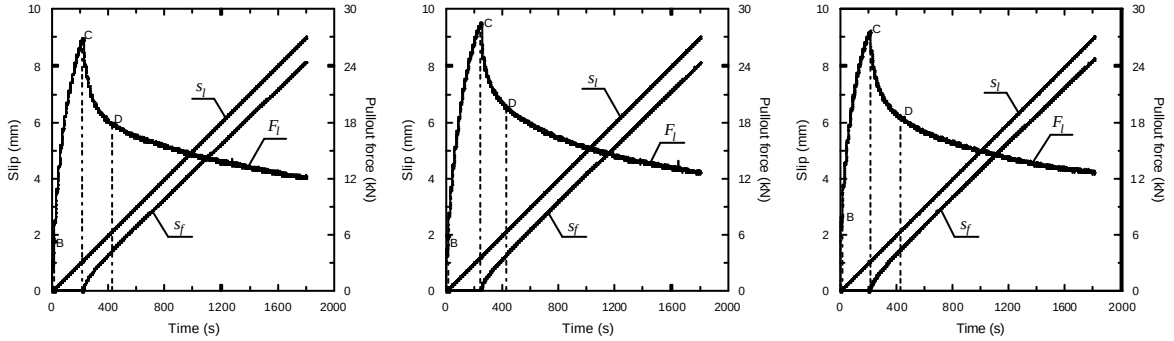

(a) (b) (c)

Figure II.12 – Time evolution of pullout force (F_l), and the slip at free end (s_f) and loaded end (s_l), of the specimen *B1_La120_M* (a), *B2_La120_M* (b) and *B3_La120_M* (c).

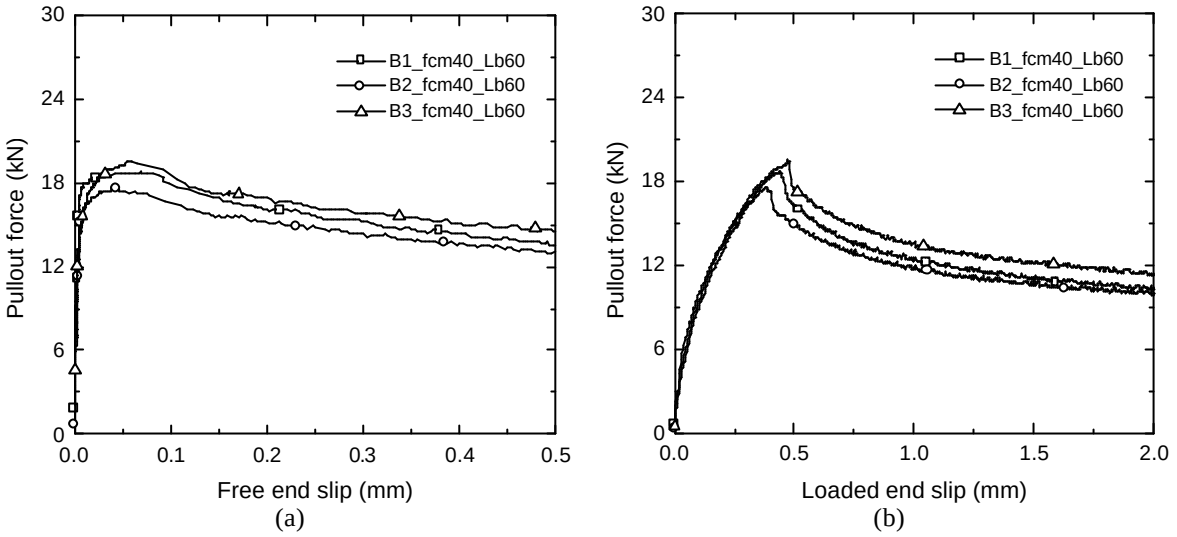

Figure II.13 – Pullout force *vs*. free end slip (a) and *vs*. loaded end slip (b), of the series *Lb60_M*.

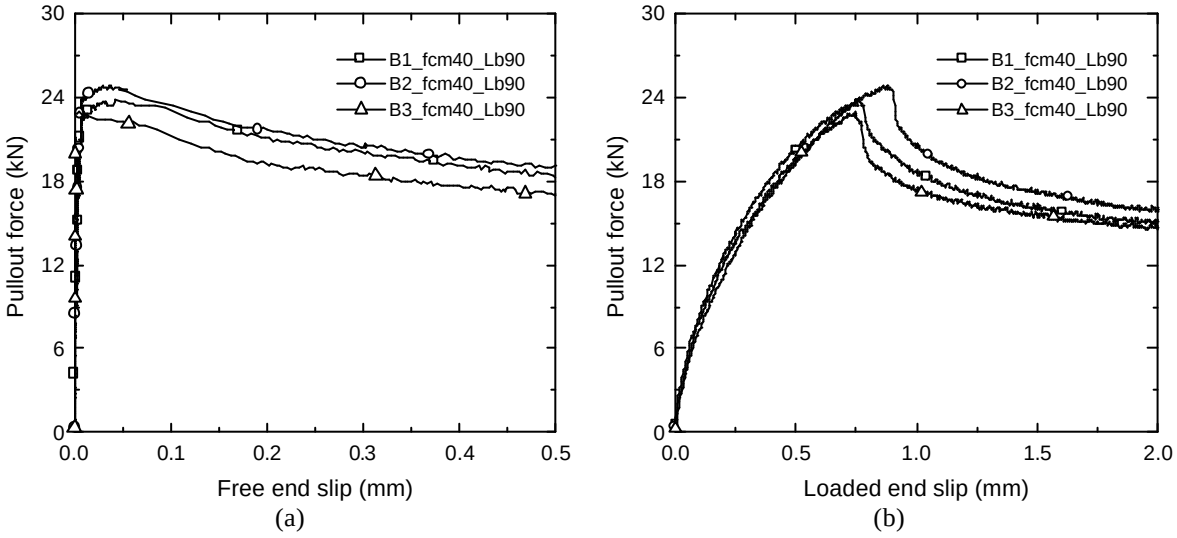

Figure II.14 – Pullout force *vs*. free end slip (a) and *vs*. loaded end slip (b), of the series *Lb90_M*.

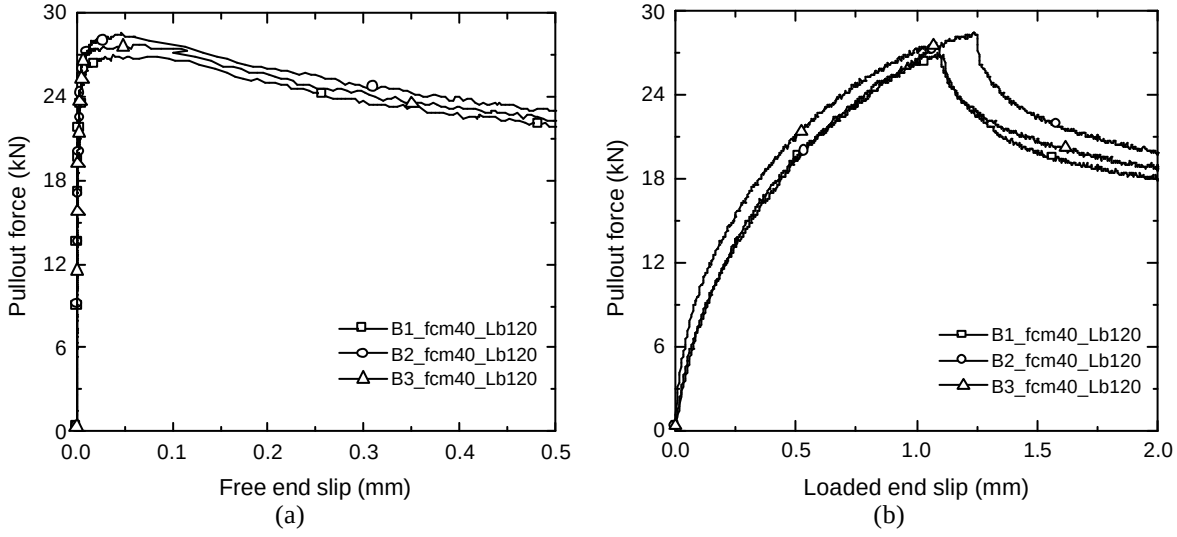

Figure II.15 – Pullout force *vs*. free end slip (a) and *vs*. loaded end slip (b), of the series *Lb120_M*.

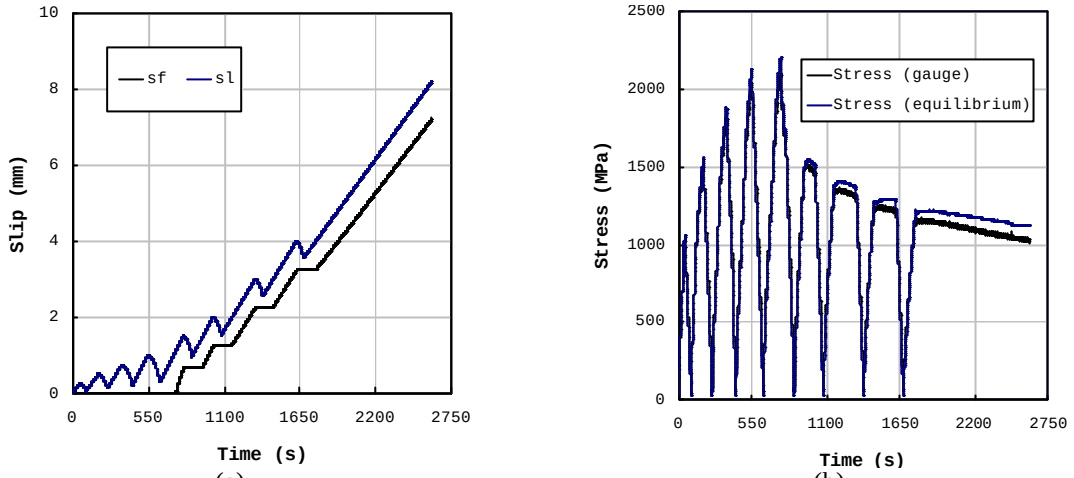

(a) (b)

Figure II.16 – Time evolution of the slip at free end (s_f) and loaded end (s_l) (a), and time evolution of the stress at the CFRP laminate of the specimen *B1_Lb120_C1*.

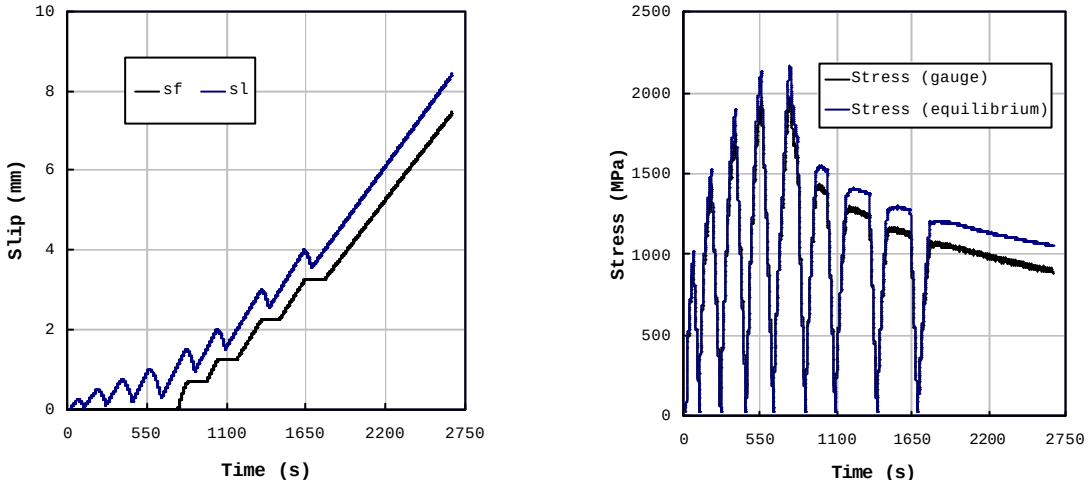

(a) (b)

Figure II.17 – Time evolution of the slip at free end (s_f) and loaded end (s_l) (a), and time evolution of the stress at the CFRP laminate of the specimen *B2_Lb120_C1*.

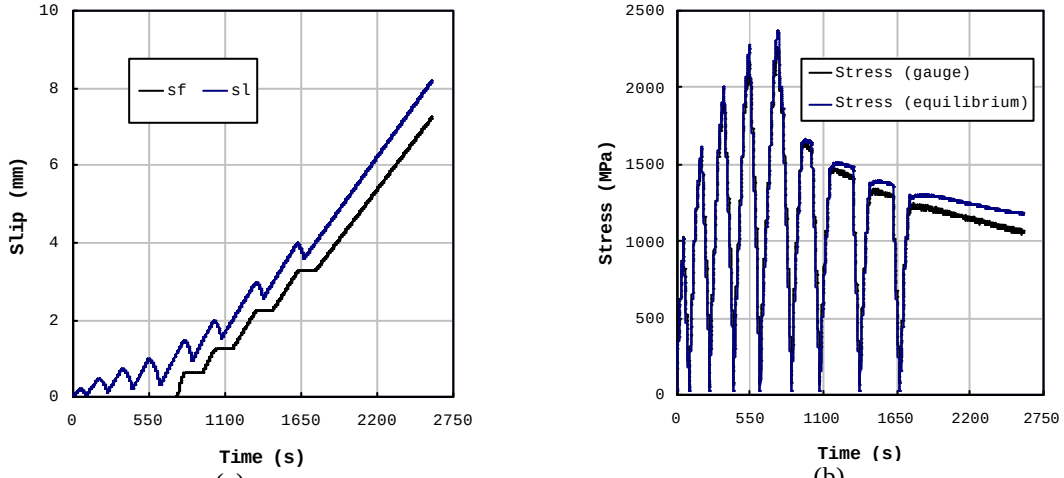

(a) (b)

Figure II.18 – Time evolution of the slip at free end (s_f) and loaded end (s_l) (a), and time evolution of the stress at the CFRP laminate of the specimen *B3_Lb120_C1*.

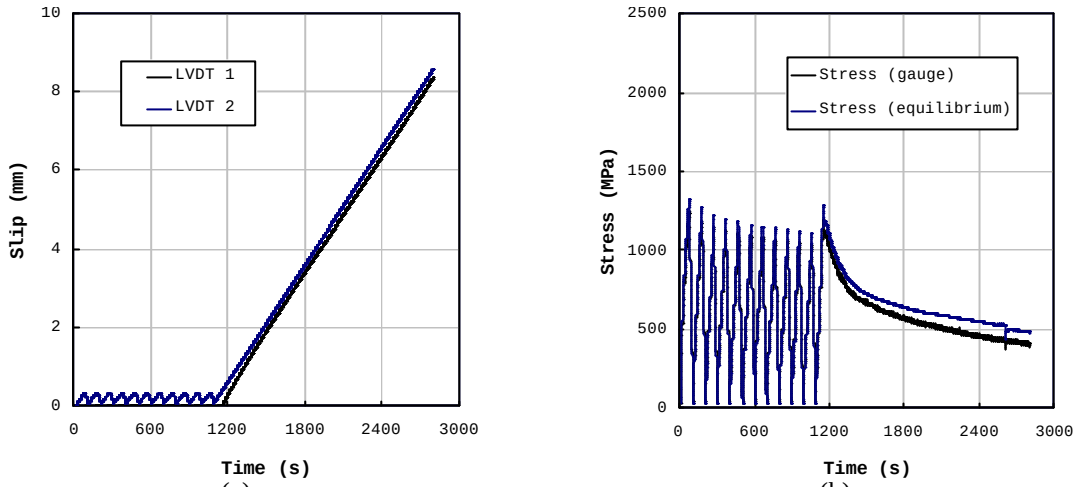

(a) (b)

Figure II.19 – Time evolution of the slip at free end (s_f) and loaded end (s_l) (a), and time evolution of the stress at the CFRP laminate of the specimen *B1_Lb60_C10*.

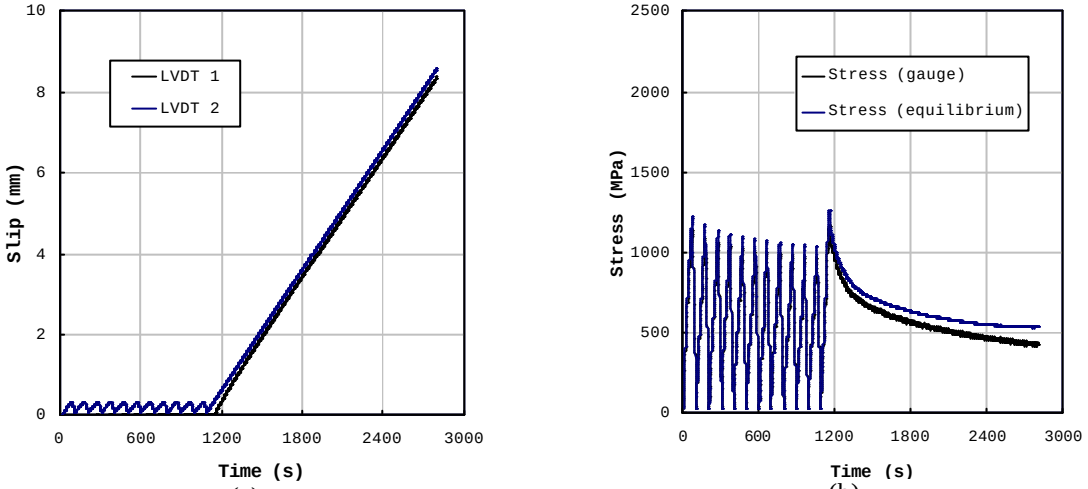

(a) (b)

Figure II.20 – Time evolution of the slip at free end (s_f) and loaded end (s_l) (a), and time evolution of the stress at the CFRP laminate of the specimen *B2_Lb60_C10*.

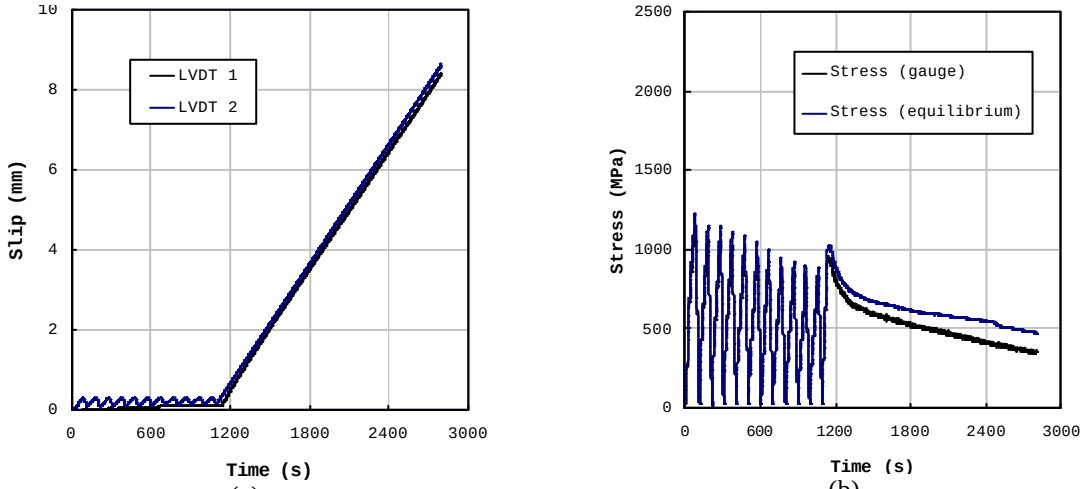

(a) (b)

Figure II.21 – Time evolution of the slip at free end (s_f) and loaded end (s_l) (a), and time evolution of the stress at the CFRP laminate of the specimen *B3_Lb60_C10*.

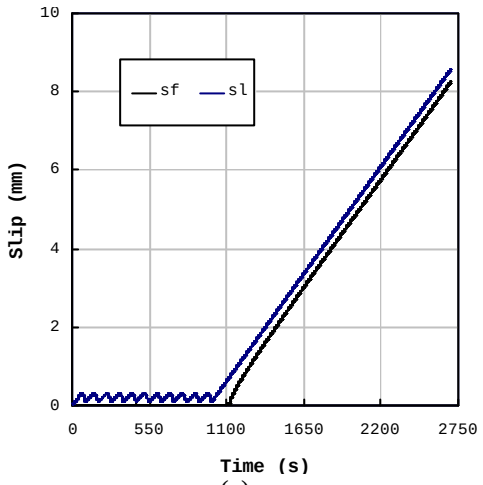

(a)

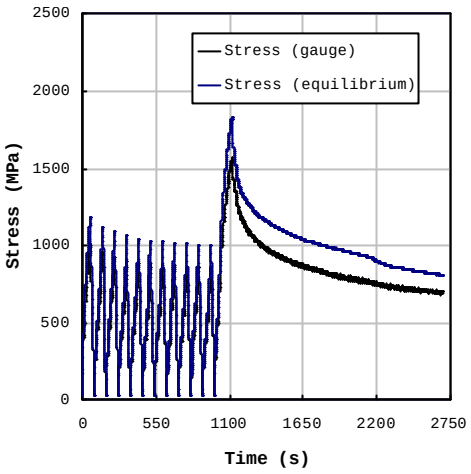

(b)

Figure II.22 – Time evolution of the slip at free end (s_f) and loaded end (s_l) (a), and time evolution of the stress at the CFRP laminate of the specimen *B1_Lb90_C10*.

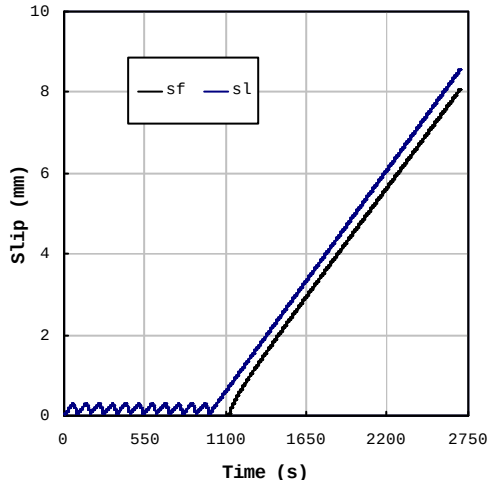

(a)

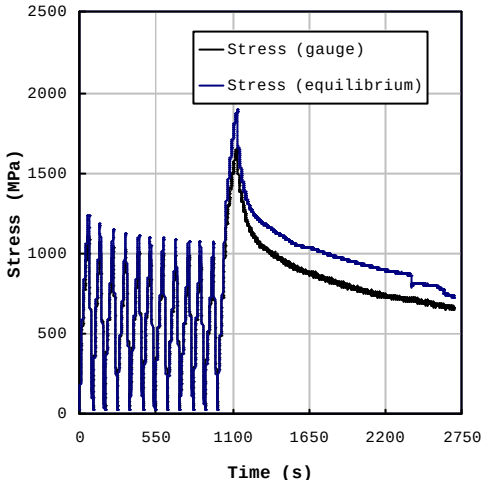

(b)

Figure II.23 – Time evolution of the slip at free end (s_f) and loaded end (s_l) (a), and time evolution of the stress at the CFRP laminate of the specimen *B2_Lb90_C10*.

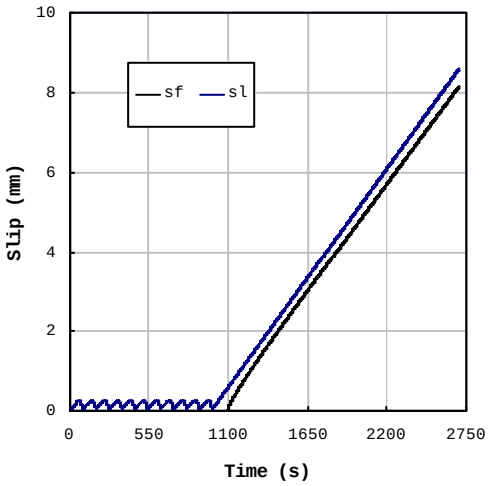

(a)

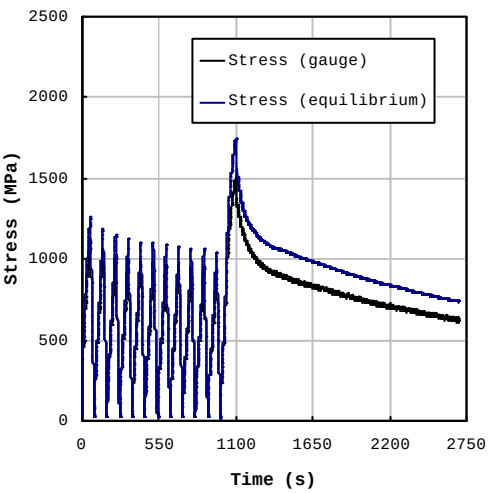

(b)

Figure II.24 – Time evolution of the slip at free end (s_f) and loaded end (s_l) (a), and time evolution of the stress at the CFRP laminate of the specimen *B3_Lb90_C10*.

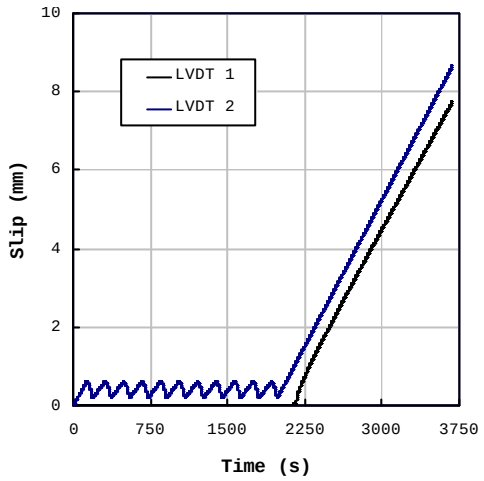

(a)

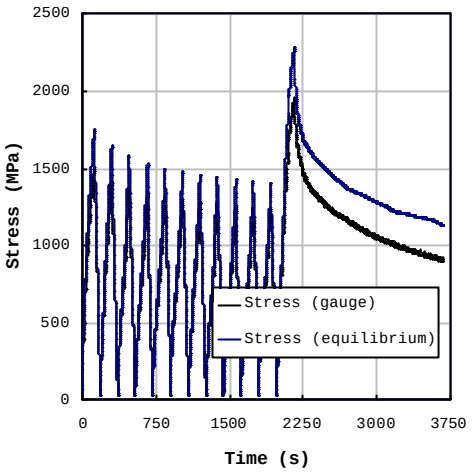

(b)

Figure II.25 – Time evolution of the slip at free end (s_f) and loaded end (s_l) (a), and time evolution of the stress at the CFRP laminate of the specimen *B1_Lb120_C10*.

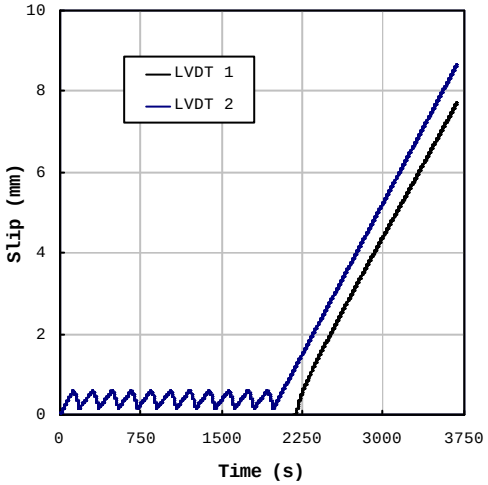

(a)

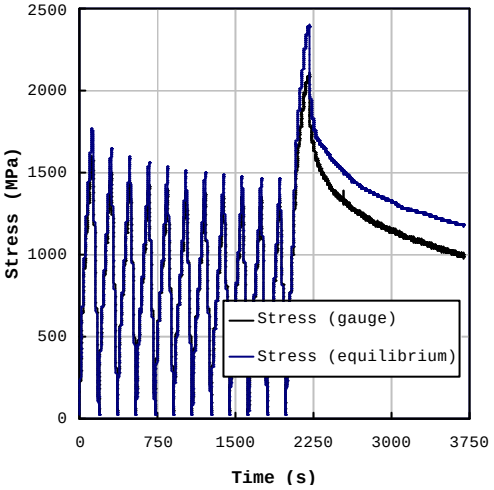

(b)

Figure II.26 – Time evolution of the slip at free end (s_f) and loaded end (s_l) (a), and time evolution of the stress at the CFRP laminate of the specimen *B2_Lb120_C10*.

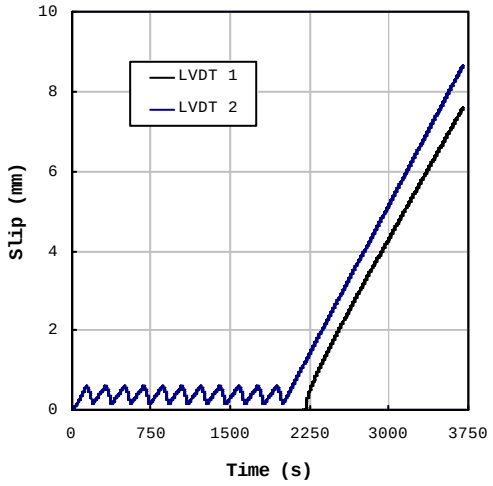

(a)

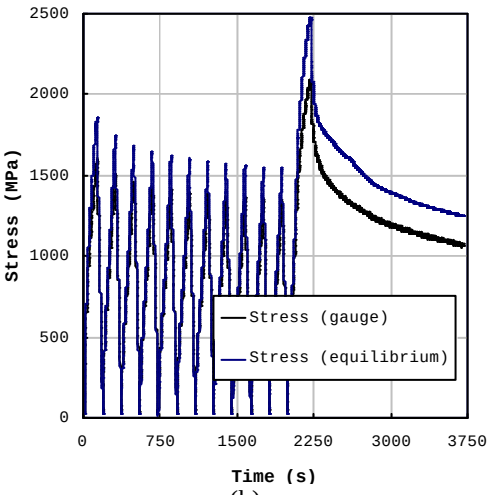

(b)

Figure II.27 – Time evolution of the slip at free end (s_f) and loaded end (s_l) (a), and time evolution of the stress at the CFRP laminate of the specimen *B3_Lb120_C10*.

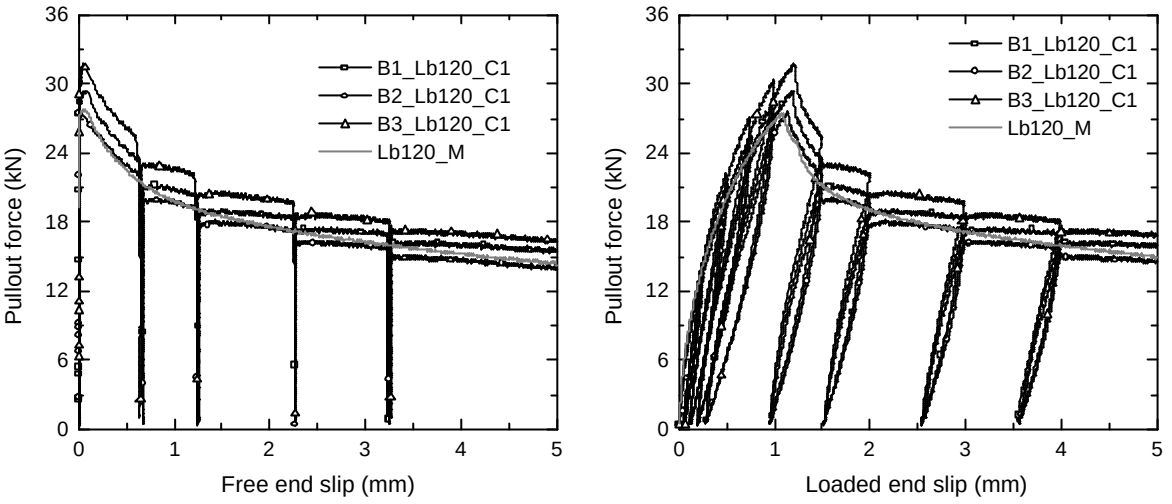

Figure II.28 – Pullout load *vs*. free end slip (a) and *vs*. loaded end slip (b), of the series *Lb120_C1*.

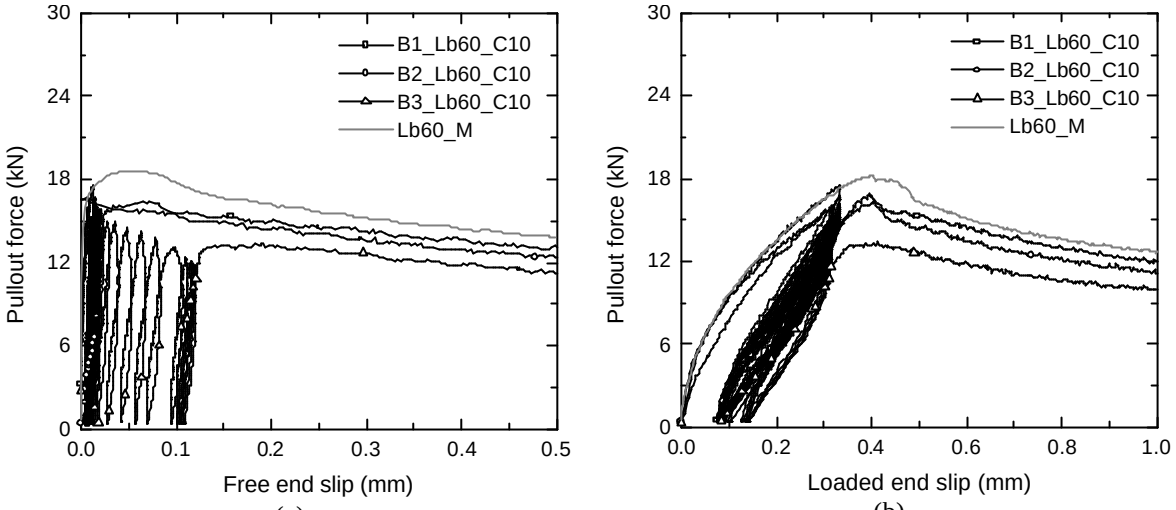

Figure II.29 – Pullout load *vs*. free end slip (a) and *vs*. loaded end slip (b), of the series *Lb60_C10*.

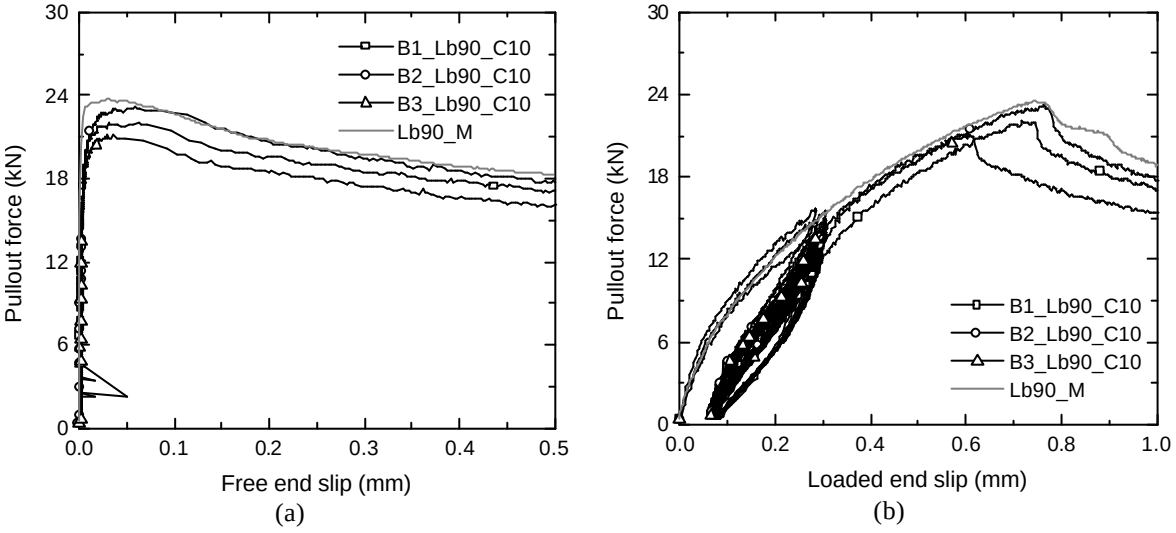

Figure II.30 – Pullout load *vs*. free end slip (a) and *vs*. loaded end slip (b), of the series *Lb90_C10*.

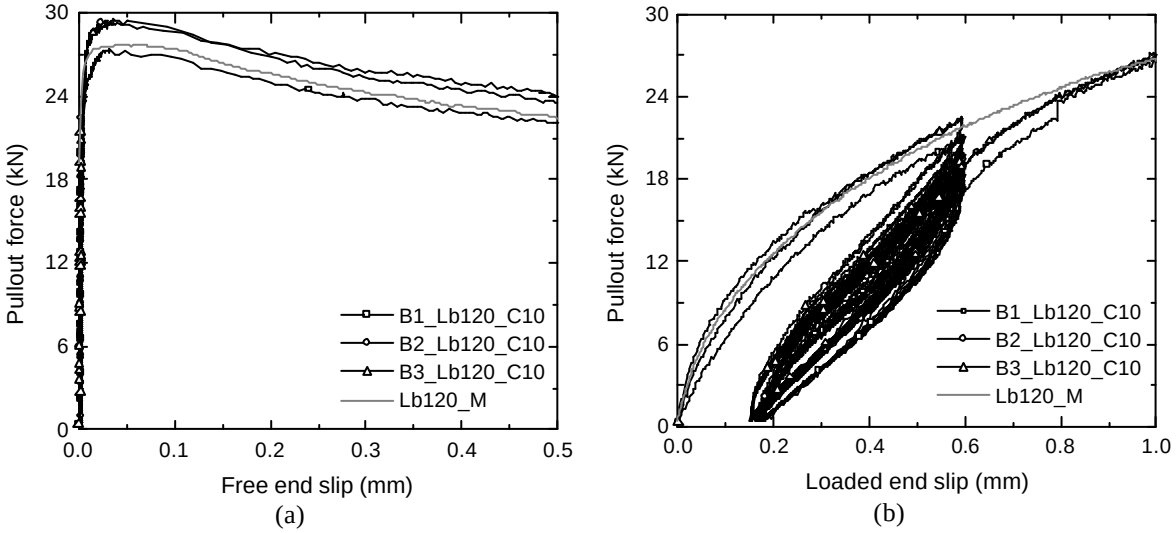

Figure II.31 – Pullout load *vs*. free end slip (a) and *vs*. loaded end slip (b), of the series *Lb120_C10*.

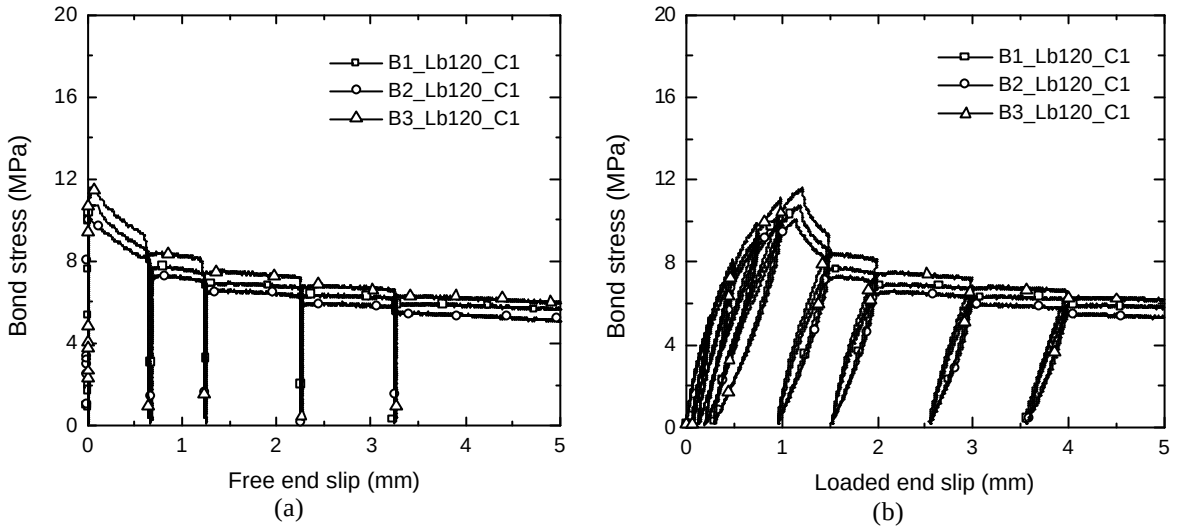

Figure II.32 – Bond stress *vs*. free end slip (a) and *vs*. loaded end slip (b), of the series *Lb120_C1*.

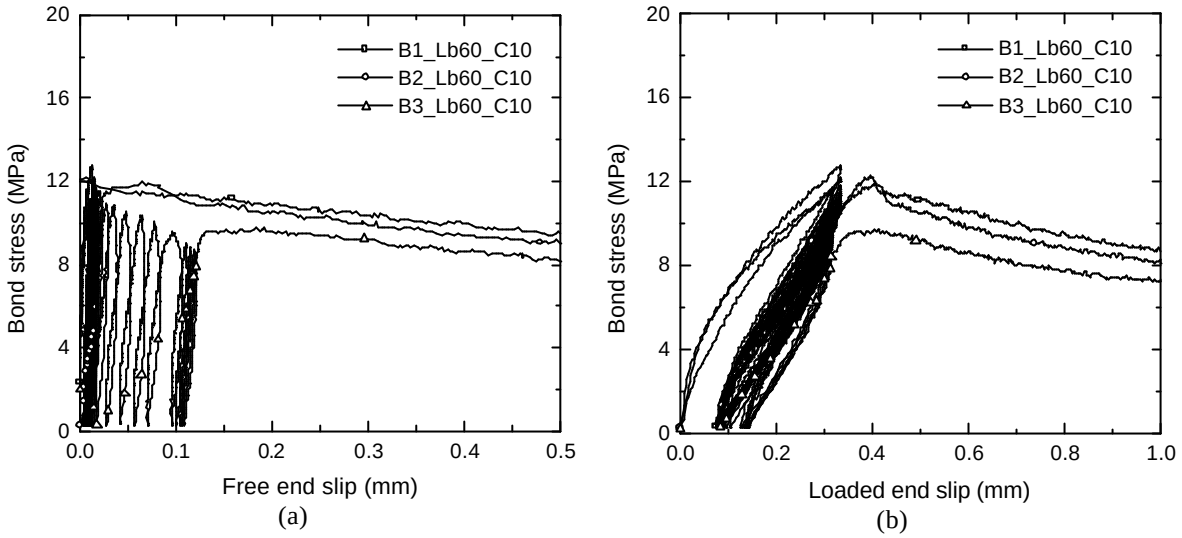

Figure II.33 – Bond stress *vs*. free end slip (a) and *vs*. loaded end slip (b), of the series *Lb60_C10*.

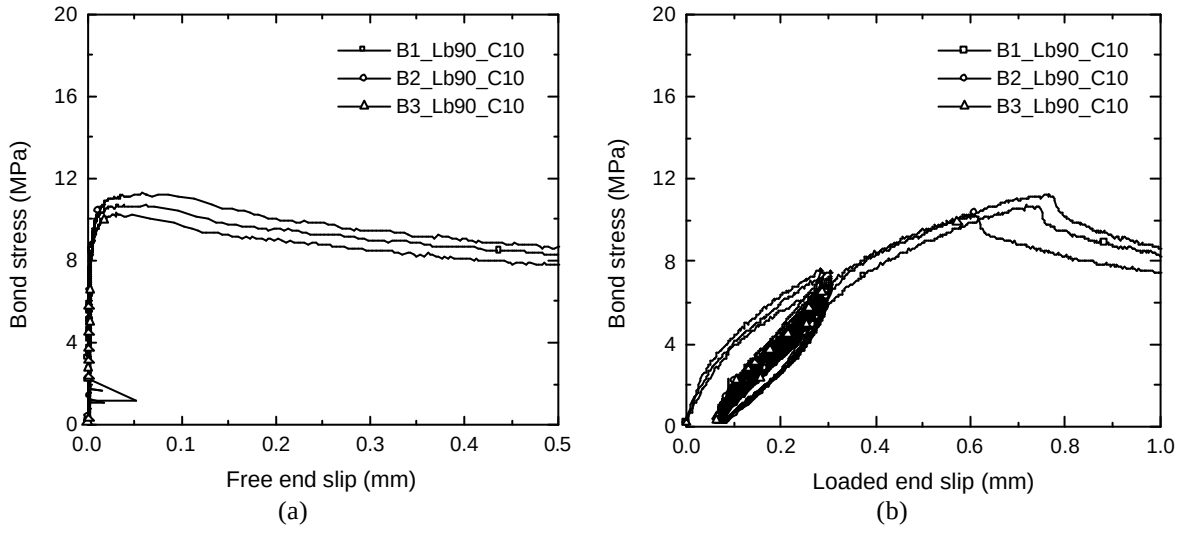

Figure II.34 – Bond stress *vs*. free end slip (a) and *vs*. loaded end slip (b), of the series *Lb90_C10*.

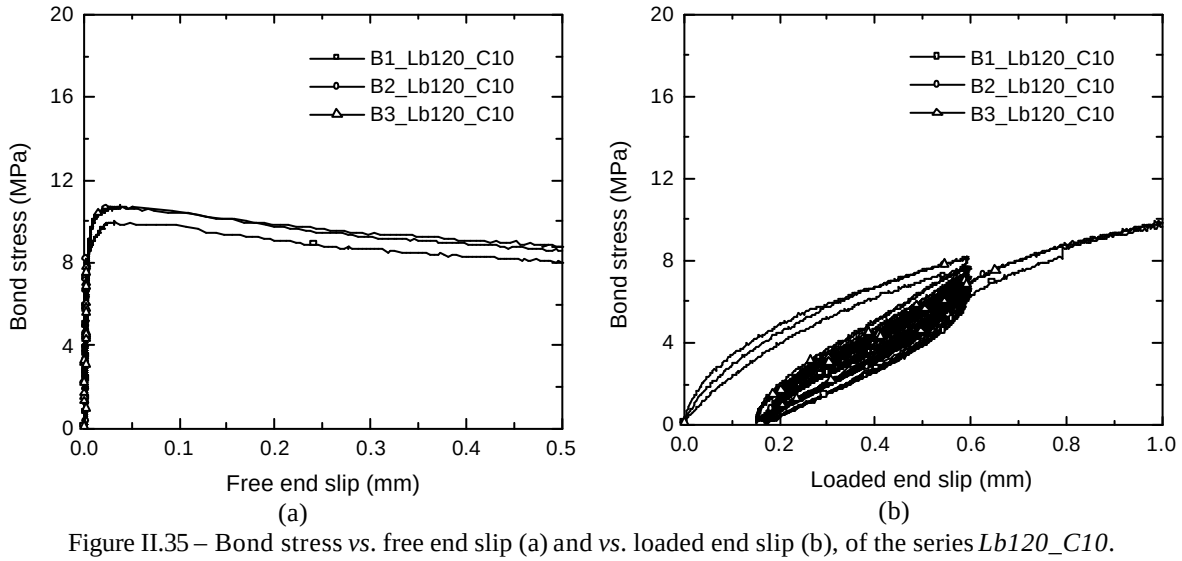

Figure II.35 – Bond stress *vs*. free end slip (a) and *vs*. loaded end slip (b), of the series *Lb120_C10*.